

RECEIVED: September 24, 2023

REVISED: December 7, 2023

ACCEPTED: December 12, 2023

PUBLISHED: December 21, 2023

Search for electroweakinos in R-parity violating SUSY with long-lived particles at HL-LHC

Biplob Bhattacharjee and Prabhat Solanki

*Centre for High Energy Physics, Indian Institute of Science,
Bengaluru 560012, India*

E-mail: biplob@iisc.ac.in, prabhats@iisc.ac.in

ABSTRACT: We investigate the R-parity violating (RPV) supersymmetric (SUSY) model at the High-Luminosity Large Hadron Collider (HL-LHC) in the context of compact muon solenoid (CMS) experiment assuming a total integrated luminosity of $\mathcal{L} = 3000 \text{ fb}^{-1}$ at $\sqrt{s} = 14 \text{ TeV}$. We focus on the pair production of electroweakinos, specifically, χ_2^0 and χ_1^\pm in wino and higgsino states in a particular scenario where χ_2^0 and χ_1^\pm decay into a Higgs boson and W boson, respectively, along the long-lived lightest supersymmetric particle (LSP), χ_1^0 , which decays to three quarks via λ'' RPV couplings leading to the prompt as well as displaced signatures in the final state. To select events at the level-1 (L1) trigger system, we employ dedicated and standard triggers followed by an offline analysis integrating information from the tracker, electromagnetic calorimeter (ECAL) and minimum ionising particle (MIP) timing detector (MTD). We observe that wino-like χ_2^0/χ_1^\pm with a mass of 1900 GeV and χ_1^0 with a mass greater than 800 GeV can be probed across a decay length ranging from 1 cm to 200 cm. In the case of higgsino-like pair production of χ_2^0/χ_1^\pm , we can probe χ_2^0/χ_1^\pm with a mass of 1600 GeV, and χ_1^0 with a mass greater than 700 GeV, across a decay length range of 1 cm to 200 cm.

KEYWORDS: Specific BSM Phenomenology, Supersymmetry

ARXIV EPRINT: [2308.05804](https://arxiv.org/abs/2308.05804)

Contents

1	Introduction	1
2	Signal model, backgrounds, and simulation setup	5
3	Triggering LLP events at L1	7
4	Offline analysis	13
4.1	Cut Based Analysis (CBA)	14
4.2	Multi Variate Analysis-1 (MVA-1)	15
4.3	Multi Variate Analysis-2 (MVA-2)	23
5	Results	27
6	Summary and conclusion	32
A	Correlation matrix for ECAL timing variables	34

1 Introduction

With a growing and urgent need to search for physics beyond the standard model (BSM), there is an ongoing effort to look for signatures of new physics in the long-lived sector on both the phenomenological and experimental sides. Numerous phenomenological studies focusing on a wide range of BSM models and signatures have been performed to search for long-lived particles (LLPs); references to some of these studies can be found here [1–22]. On the experimental side, LHC’s two general-purpose detectors, ATLAS and CMS, have been actively searching for displaced signatures at the colliders. Studies done at ATLAS and CMS look for a wide range of experimental signatures using vertex and non-vertex-based methods. For vertex-based searches, signatures include displaced jets, vertices, and leptons. On the other hand, non-vertex-based searches feature signatures such as emerging jets, trackless jets, disappearing tracks, non-pointing photons, and jets with low electromagnetic energy fractions. CMS [23–38] and ATLAS [39–58] have extensively documented these studies. Along with CMS and ATLAS, LHCb has also carried out numerous LLP searches involving displaced jets, dark photons and displaced leptons [59–65]. Significant efforts are also being intensively made in the field of hardware development to improve the detection of LLPs at the large lifetime frontier. This includes the development of new detectors like FASER [66], MATHUSLA [67, 68] and CODEX-b [69, 70], and hardware specifically designed for search of displaced physics at the LHC’s general purpose detectors along with application of innovative analysis techniques that utilise a variety of information from the different sub-detectors at HL-LHC. There are several proposals for dedicated detectors for LLP searches at future colliders like FCC-ee [71, 72]. For FCC-hh, a transverse detector, DELIGHT [19], and a forward detector, FOREHUNT [73] have been proposed.

In the context of LLPs, Supersymmetry (SUSY) [74–76] has been one of the most studied BSM theories. In MSSM, conservation of R-parity [77] ensures that SUSY particles can be pair-produced with odd R-parity where the decay of each of them should lead to an odd number of sparticles and the lightest SUSY particle (LSP) is stable. Numerous studies have investigated the phenomenological implications of R-parity conserving (RPC) scenarios [78–94]. Although, R-parity conservation is required to avoid unwanted B- and L- violating effects [95, 96] such as proton decay but it is not the utmost requirement as presence of some other symmetries can allow R-parity violation (RPV) while forbidding proton decay [97–100]. All standard model particles are assigned $R_p = 1$ while their super-partners are assigned $R_p = -1$.

A viable MSSM superpotential comprising of gauge invariant and R-parity violating terms [101, 102] can be constructed as follows,

$$W = \mu_i H_u L_i + \frac{1}{2} \lambda_{ijk} L_i L_j E_k^c + \frac{1}{2} \lambda'_{ijk} L_i Q_j D_k^c + \frac{1}{2} \lambda''_{ijk} U_i^c D_j^c D_k^c \quad (1.1)$$

where λ_{ijk} , λ'_{ijk} and λ''_{ijk} are various RPV yukawa couplings with i, j, k being generation indices. E, U and D represent the superfields for right-handed lepton, up-type quark and down-type quark, respectively, while L and Q correspond to left-handed lepton and quark superfields, respectively, while H_u represent superfield for up-type Higgs. In the current study, we only focus on λ''_{ijk} Yukawa coupling, where a sparticle decays to quarks with very small coupling leading to the sparticle being long-lived. Examples of such LLPs in the context of MSSM can be electroweakinos (χ_1^\pm , χ_2^0 and χ_1^0) and gluinos. Various experiments have set an upper limit on RPV couplings to be very small, leading to SUSY particles being produced with longer lifetimes. In [103], where bounds on λ''_{ijk} are calculated from double nucleon decay into two kaons, λ''_{112} less than $10^{-15} R^{-5/2}$ is excluded where R represents ratio between hadronic and supersymmetric scales and can vary from 10^{-3} to 10^{-6} . Accordingly, λ''_{112} can vary from value as low as 10^{-7} to 1. Indirect bound on λ''_{113} comes from neutron oscillations where λ''_{113} less than 10^{-4} is excluded for $m_{\tilde{g}} = 100$ GeV [104].

Several displaced jet searches have been performed at CMS and ATLAS to set exclusion limits specifically on the mass, lifetime, and production cross-section of LLPs decaying to jets assuming different SUSY models. CMS has conducted studies on RPC SUSY scenarios involving LLPs, setting constraints on their production. Detailed results and models are elaborated in the reference [34].

For the RPV SUSY model where gluinos are pair-produced with each gluino decaying to a top, bottom and strange quark through λ''_{323} type UDD coupling, CMS rules out gluino pair production cross-section exceeding 0.1 fb when $c\tau$ ranges between 3 and 1490 mm and $m_{\tilde{g}}$ is 2400 GeV. Between $c\tau$ 3 mm and 1000 mm, gluinos up to 2500 GeV mass are excluded [34]. CMS also studies two other RPV models where top squarks are pair-produced, and each squark subsequently decays to a lepton and a bottom or a down type quark via λ'_{x33} or λ'_{x31} LQD type RPV coupling. For the RPV model with λ'_{x33} LQD type coupling, production cross-sections of a stop above 0.1 fb are excluded for $c\tau$ between 8 mm and 160 mm for $m_{\tilde{t}} = 1600$ GeV. For $c\tau$ between 5 mm and 240 mm, top squark masses up to 1600 GeV are excluded [34].

For the RPV model with λ'_{x31} LQD type coupling, stop production cross-sections exceeding 0.1 fb are excluded for $c\tau$ between 7 mm and 220 mm for $m_{\tilde{t}} = 1600$ GeV. Top squark masses up to 1600 GeV are excluded for $c\tau$ between 3 mm and 360 mm [34]. Another study done at

CMS to study nonholomorphic RPV coupling where top squarks undergo pair-production and then decay to two down type anti-quarks each, for a top squark mass $m_{\tilde{t}} = 1600$ GeV, the production cross sections exceeding 0.1 fb are ruled out for $c\tau$ ranging between 3 mm and 820 mm. Additionally, for $c\tau$ values between 2 mm and 1320 mm, top squark masses up to 1600 GeV are excluded [34].

A recent study performed at the ATLAS experiment has set up very stringent exclusion limits on masses of displaced electroweakinos in two benchmark scenarios of LLPs decaying to jets via UDD-type RPV coupling [58]. In the first scenario, electroweakinos are pair-produced in pure higgsino state which includes four possible combinations of electroweakinos: $\chi_1^\pm \chi_2^0$, $\chi_2^0 \chi_1^0$, $\chi_1^+ \chi_1^-$ and $\chi_1^\pm \chi_1^0$ while the other scenario involves pair-production of gluinos (\tilde{g}) where each gluino decays promptly to a long-lived neutralino and a quark and anti-quark pair with 100% branching ratio. In each scenario, electroweakinos decay to light flavour quarks via the λ'' coupling with 100% branching ratio. Electroweakinos with masses less than 1500 GeV are excluded for mean proper lifetime between 0.03 ns ($c\tau = 9$ mm) to 1 ns ($c\tau = 300$ mm) for pair-produced electroweakinos, while electroweakinos with masses less than 1500 GeV are excluded for mean proper lifetime between 0.02 ns ($c\tau = 6$ mm) to 4 ns ($c\tau = 1200$ mm) for electroweakinos produced through the decay of gluinos with a mass of 2.4 TeV. In the context of the present analysis concerning pair-produced electroweakinos, we observe weaker limits as we increase the decay length of the LLPs above 30 cm. We summarise the current stringent limits on RPV SUSY models as discussed above for various SUSY particles in mass and decay length plane in table 1.

In conclusion, as we can see from the table 1, based on the displaced searches performed at both CMS and ATLAS, we observe that exclusion limits set for the masses of displaced gluinos are significantly high, with gluinos having mass up to 2.5 TeV already excluded at CMS [34]. However, the limits imposed on the mass of displaced electroweakinos are moderate and can still be probed at future colliders like HL-LHC [105]. It is also important to highlight that while we observe stronger limits for LLPs with smaller lifetimes, the limits placed on the electroweakinos are considerably lenient for highly displaced ones. For example, in the scenario described in [58], where electroweakinos are pair-produced with a decay length of about 500 cm, the excluded electroweakino mass reduces from 1500 GeV to roughly 1050 GeV.

In this paper, we exclusively focus on the CMS detector at HL-LHC, one of the general-purpose detectors that will undergo several major hardware and software upgrades. At the HL-LHC, the peak instantaneous luminosity is set to rise to 5×10^{34} (7.5×10^{34}) $\text{cm}^{-2}\text{s}^{-1}$, with each pp collision witnessing 140 (200) pile-up interactions [105]. HL-LHC is projected to record data corresponding to an integrated luminosity of 3000 (4000) fb^{-1} during its lifetime [105]. In order to deal with increased PU interactions and maintain the optimal physics performance of the detectors, several hardware upgrades will take place, starting with the upgrade of trigger and data acquisition systems (DAQ). With the upgrade of both the inner and outer tracker and the implementation of Field Programmable Gate Arrays (FPGA), there will be a significant overhaul in the data acquisition process at level-1 (L1) of the trigger system [106]. This upgrade enables the availability of tracking information at L1. Additionally, calorimeter information from ECAL and HCAL will also be made available at L1 [106]. The improved data acquisition and processing architecture at L1 will make it possible to implement

Process/Decay	Coupling	Particle	$c\tau$ (mm)	Mass Excl. (GeV)	Reference
$pp \rightarrow \tilde{g}\tilde{g}/\tilde{g} \rightarrow tbs$	λ''_{323}	\tilde{g}	3-1000	2500	[34]
$pp \rightarrow \tilde{t}\tilde{t}/\tilde{t} \rightarrow lb$	λ'_{x33}	\tilde{t}	5-240	1600	[34]
$pp \rightarrow \tilde{t}\tilde{t}/\tilde{t} \rightarrow ld$	λ'_{x31}	\tilde{t}	3-360	1600	[34]
$pp \rightarrow \tilde{t}\tilde{t}/\tilde{t} \rightarrow dd$	η''_{311}	\tilde{t}	2-1320	1600	[34]
$pp \rightarrow \chi\chi/\chi \rightarrow qq\bar{q}$	λ''_{x11}	χ	9-300	1500	[58]
$pp \rightarrow \tilde{g}\tilde{g}/\tilde{g} \rightarrow \chi_1^0 + q\bar{q}$	λ''_{x11}	χ_1^0	6-1200	1500	[58]

^a l and x denote leptons and generation indices respectively, χ denotes electroweakinos ($\chi_1^+, \chi_1^-, \chi_2^0, \chi_1^0$), q denote light-flavour quarks (u, d).

Table 1. Summary of the RPV SUSY model exclusion limits from CMS and ATLAS.^a

particle flow and machine learning techniques, along with higher-level object reconstruction, to be used in the trigger system. This will be immensely helpful in recording rare BSM events, such as events containing displaced objects, that would have otherwise gone unrecorded. The implementation of extended tracking at L1 will enable the reconstruction of displaced tracks up to a certain transverse impact parameter, which will again be very helpful in selecting events with displaced signatures at L1. Displaced particle searches will also benefit from the availability of timing information from the upgraded ECAL at L1 [106, 107] and the inclusion of an all-new MIP timing detector (MTD) between the tracker and calorimeter system [108]. Additionally, a new high granularity calorimeter (HGCal) will replace the existing endcap calorimeter [109], enhancing the physics performance in the forward region under the harsher conditions at the HL-LHC.

The upgrades planned for the HL-LHC will substantially boost physics sensitivity and increase the probing potential of LLPs at HL-LHC. However, there are not many comprehensive and realistic phenomenological studies explicitly designed for HL-LHC that fully consider the effect of increased PU and make the most of the impending hardware upgrades at HL-LHC. This motivates us to investigate the lifetime frontier of BSM physics in the context of RPV SUSY, considering increased PU conditions at HL-LHC.

The rest of the paper is structured as follows: in section 2, we outline the signal model, background sources, and the simulation setup for both signal and background events. Section 3 explains the implemented triggering strategy at L1, where we select events at L1 by utilising available information from the upgraded detector systems. In section 4, we perform a detailed analysis of the events selected at L1. This analysis involves studying various physics variables constructed using offline information from different sub-detectors at the CMS. The analysis is divided into three parts: a cut-based analysis and two independent multi-variate analyses. Section 5 presents the signal significance for various LLP benchmark points, providing quantitative results for our analysis. Finally, in section 6, we summarise and draw conclusions based on our analysis.

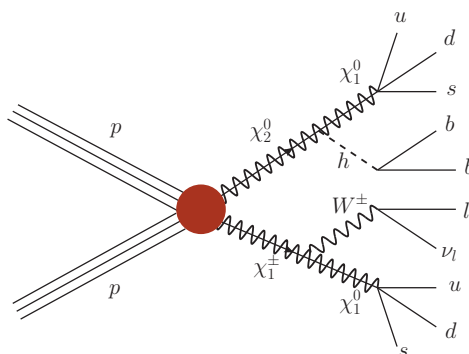


Figure 1. Feynman diagram of cascade decay of electroweakinos (χ_2^0/χ_1^\pm) where χ_2^0 decays to χ_1^0 and 125 GeV Higgs boson while χ_1^\pm decays to a W boson and χ_1^0 .

2 Signal model, backgrounds, and simulation setup

In this paper, we study R-parity violating Yukawa coupling of type λ'' within the framework of MSSM. Our focus is on the associated production of electroweakinos, specifically the χ_2^0 and χ_1^\pm where χ_2^0 decays to lightest supersymmetric particle (LSP), χ_1^0 , and the 125 GeV Higgs boson while the χ_1^\pm decays to a W-boson and χ_1^0 . Due to a very small λ'' coupling, the χ_1^0 exhibits a long lifetime. We consider the decay of χ_1^0 to light flavour quarks (u, d, and s) with a 100% branching ratio. We assume a 100% branching fraction for the decays $\chi_2^0 \rightarrow \chi_1^0, h$ and $\chi_1^\pm \rightarrow \chi_1^0, W^\pm$. The inclusive decays of the Higgs boson and W boson are considered, with their respective branching ratios taken from [110]. Quarks resulting from the decay of χ_1^0 undergo showering and hadronisation, leading to the production of multiple displaced jets in the final state. Feynman diagram illustrating the cascaded decay process assuming only one decay mode for both Higgs boson and W boson is shown in figure 1. In this diagram, the Higgs boson decays exclusively into two b-jets, while the W boson decays into leptons.

The pair production cross-section of the neutralino-chargino pair at $\sqrt{s} = 14$ TeV is calculated at the next-to-leading order (NLO) with the incorporation of next-to-leading-log (NLL) effects, using the RESUMMINO code [111]. For the current analysis, we solely focus on the pair production of electroweakino with degenerate masses ($m_{\chi_2^0} = m_{\chi_1^\pm}$). The SUSY cross-sections for electroweakino pair production provided by the LHC SUSY cross-section working group [112] matches with those we got from RESUMMINO.¹

We study LLPs, χ_1^0 , in a mass range varying from 500 GeV to 1 TeV, with mean proper decay length varying from 1 cm to 500 cm. For signal generation, as well as for showering and hadronisation, we utilise PYTHIA 8.308 [113]. The signal samples are generated using the CTEQ6L1 PDF (Parton Distribution Function) [114] with the CUETP8S1-CTEQ6L1 CMS tune [115]. During the sample generation, we adjust the decay width of the LLPs in the input SLHA (Supersymmetry Les Houches Accord) file to modify the decay length of the LLPs.

The primary background in our study, featuring multiple jets in its final state, is predominantly due to instrumental effects. These include multi-hadronic noise from various

¹RESUMMINO gives cross-sections of 0.124 fb for 1500 GeV wino-like and 0.051 fb for 1400 GeV higgsino-like electroweakino pair production. In comparison, the LHC SUSY Cross-Section Working Group lists these cross-sections as 0.12 fb and 0.05 fb, respectively, for the same processes.

interactions with detector components. Another dominant source of background is QCD multijet processes. Additionally, due to the presence of leptons in the final state, a subdominant contribution to the background comes from $t\bar{t}$ events in which the top quark can decay leptonically or hadronically. We also anticipate background contribution from W +jets events, where the W boson decays inclusively. Here, we would like to mention that simulating and characterising the instrumental effects are out of the scope of the current study. Instead, we focus on the mitigation strategy for the instrumental background outlined in the subsequent sections.

QCD events are generated in the bins of parton level H_T (H_T^{gen}). Here, H_T^{gen} is calculated by summing the transverse momenta of all partons involved in the event. H_T^{gen} bins used in this study include the following ranges: 500–600 GeV, 600–700 GeV, 700–800 GeV, 800–1000 GeV and >1000 GeV. H_T^{gen} bins are selected based on the analysis strategy, where events in the offline stage of the study after being triggered at level-1 by the triggers, as elaborated in section 3, are required to have high event H_T . This is because signal events can easily surpass the $H_T > 500$ GeV threshold due to significant hadronic activity in the final state. Therefore, QCD multijet events are generated in H_T^{gen} bins starting with $H_T^{gen} > 500$ GeV in order to ensure sufficient background statistics. Generation of background events is done in `madgraph` [116, 117] while showering is done using `PYTHIA 8.308`.

We use `Delphes-3.5.0` [118] for simple detector simulation. To replicate the conditions at HL-LHC accurately, which are characterised by a high PU environment, our analysis takes into account the effects of PU. PU originates from the multiple soft proton-proton interactions that occur within a single bunch crossing, along with a hard collision. We use `PYTHIA 8.308` to generate 1 million soft QCD events, which are utilised as PU events. The `PileUpMerger` module in `Delphes` subsequently merges these PU events with the hard process. Both signal and background events have an average of 140 PU events.

We use the default CMS card provided with `Delphes` for HL-LHC for detector simulation. However, we make specific modifications to certain `Delphes` modules as elaborated in one of our previous studies [10]. To form jets using energy deposits from the calorimeters, ECAL and HCAL, we use the anti- k_T jet clustering algorithm [119] with a cone size of $R = 0.3$. Using a narrower jet cone size instead of the standard $R = 0.4$ was motivated by the need to mitigate contamination from PU interactions, which can significantly affect the measurement of physics variables. The amount of PU contamination within a jet relies on the jet area, as PU is distributed throughout the detector. A reduction in the jet area leads to a smaller PU contribution. By shrinking the jet cone size, the effects of PU can be effectively reduced, assuming that the jets from the signal process remain unaffected and that the majority of the hadronic activity from the signal is captured within a reduced cone radius. This approach aligns with our analysis, as prior studies [3, 5, 9, 10] have shown that displaced jets resulting from LLP decays typically concentrate energy within a more confined region of the $\eta - \phi$ plane. In [9, 10], we have explicitly shown the effect of the narrow cone size of a jet on jet variables like jet p_T , track multiplicity within a jet, as well as on timing of jet where narrow cone size evidently reduces the adverse effect of PU on jet variables. Consequently, opting for a narrow jet cone size for jets can aid in minimising the impact of PU on LLP jets. Therefore, we opt for a narrow cone size of $R = 0.3$ compared to standard $R = 0.4$.

Before we proceed further, let's define two signal benchmark points (BP) for our analysis,

- **BP-1:** $M_{\chi_2^0}/M_{\chi_1^\pm} = 1600$ GeV, $M_{\chi_1^0} = 800$ GeV, and $c\tau = 10$ cm.
- **BP-2:** $M_{\chi_2^0}/M_{\chi_1^\pm} = 1600$ GeV, $M_{\chi_1^0} = 800$ GeV, and $c\tau = 100$ cm.

Here, $c\tau$ represents the mean proper decay length of the LLP. We have selected benchmark points (BP-1 and BP-2), keeping in mind the stringent limit on the masses of electroweakinos. Both BP-1 and BP-2 feature moderately heavy LLPs resulting from the decay of significantly heavy electroweakinos, $M_{\chi_2^0}/M_{\chi_1^\pm} = 1600$ GeV. These electroweakinos have an extremely small pair-production cross-section. We are examining two decay length scenarios: one involves a shorter decay length of 10 cm, and the other features a considerably longer decay length of 100 cm, for which the limits are still lenient. Throughout the rest of the paper, we will use the aforementioned shorthand notation to refer to the signal benchmark points. QCD events with $H_T^{gen} \in \{500, 600\}$ GeV will be represented as “QCD,” and top quark pair events will be denoted as “ $t\bar{t}$ ”. We generate 5 million $t\bar{t}$ events, 3 million QCD dijet events spread across the mentioned H_T^{gen} bins, and 0.6 million W+jets events. For each signal benchmark point, 0.5 million events are generated. The generation and analysis of large background datasets involving 140 PU interactions present a significant challenge. The size of the simulated events using `Delphes`, including only tracks, towers, and jet branches, can reach up to 15 GB for 5000 events. This makes it impractical to produce extensive background datasets that surpass what we have already generated due to our computational limitations.

3 Triggering LLP events at L1

The CMS experiment employs a two-level trigger system, consisting of the Level-1 (L1) and the High-Level Trigger (HLT), to identify and select interesting events for offline analysis [106, 120–122]. The HLT is a software-based trigger, while the L1 trigger is a hardware-based system with an extremely short latency period that determines the time window within which the decision to record an event is made. Because of this low latency period, performing complex physics calculations and constructing high-level physics objects using information from multiple sub-detectors can be challenging and inefficient. However, with the proposed upgrades to the data acquisition system, it becomes possible to reconstruct certain high-level physics objects and apply machine-learning (ML) techniques at the L1 trigger stage in the context of the HL-LHC. (For more comprehensive information about the implementation of ML algorithms at FPGAs, please refer to [123, 124] and references therein). These upgrades will involve increasing the latency period and enhancing the data bandwidth, measured in terms of event rate. These improvements will enable the design of triggers aimed explicitly at searching for LLPs. Therefore, it is crucial to efficiently utilise available resources to select events at L1 that do not overlook exotic LLP events, which typically have a very small cross-section. The final state signature for our study consists of displaced jets and prompt leptons. Our primary focus will be on triggering events using dedicated triggers to detect events containing these specific physics objects.

At the HL-LHC, CMS has proposed two dedicated triggers explicitly designed to select events with a displaced jets signature [106]. In addition to these dedicated LLP triggers,

single-lepton triggers can further maximise the trigger efficiency [11]. We will explain the triggers used in our analysis in detail below,

- **Track- H_T** : at the HL-LHC, CMS plans to upgrade the inner tracker by replacing both the pixel and strip tracking detectors with smaller pixel sensors. The outer tracker will also be improved by incorporating strip and macro pixel sensors with stacked strip modules. The main requirements for the upgraded tracker system at HL-LHC include high radiation tolerance, increased granularity, improved track separation, availability of tracking information at L1, and extended tracking acceptance. The upgraded outer tracker will facilitate the reconstruction of track candidates at L1, operating at a rate of 40 MHz, for $|\eta| < 2.4$. This will be achieved through an increased latency period and the implementation of FPGAs, enabling the construction of track-based triggers at L1. The availability of tracking information at L1 will warrant the identification of the primary vertex and will be immensely useful in mitigating charged PU. In addition to the advantages mentioned above of including tracking information at L1, one particular advantage relevant to this analysis is the extension of the L1 tracking algorithm to reconstruct tracks displaced within the detector. Our analysis considers a track displaced from the beamline if it has a transverse impact parameter ($|d_0|$) greater than 1.5 mm. These tracks may originate from a secondary vertex following the decay of an LLP. The efficiency of track reconstruction for displaced tracks at L1 will depend on the $|d_0|$ of the tracks, with efficiency decreasing as $|d_0|$ increases. Tracking at L1 will be available for particles with transverse momentum (p_T) greater than 2 GeV within the pseudorapidity ($|\eta|$) range of less than two. It will follow a track reconstruction efficiency curve as shown in the reference [106].

To highlight the importance of displaced tracking at L1, figure 2 illustrates the L1 displaced track multiplicity within a $\Delta R < 0.3$ cone around the jet axis for two LLP benchmark scenarios: BP-1 (decay length of 10 cm) and BP-2 (decay length of 100 cm), with $M_{\chi_1^0} = 800$ GeV and $M_{\chi_2^0} = 1600$ GeV for jets with $p_T > 40$ GeV and $|\eta| < 2.5$. The figure also shows the displaced track multiplicity for two primary background sources: $t\bar{t}$ and QCD dijet events.

The figure underlines the importance of displaced tracks within jets for distinguishing between long-lived signal and background events, as we observe that the displaced track multiplicity is significantly lower for the backgrounds compared to the signal benchmark points. Moreover, the LLP benchmark (BP-1) with a shorter mean proper decay length of 10 cm exhibits a higher number of reconstructed displaced tracks, which is evident from the longer tail observed in the multiplicity distribution compared to the benchmark with a longer decay length (BP-2). This observation aligns with our expectations, as LLPs with longer decay lengths will have a larger value of $|d_0|$ and, therefore, fewer displaced tracks will be reconstructed.

CMS has proposed a dedicated trigger for LLPs called “Track- H_T ” to identify events with displaced jets originating from LLPs using the upgraded tracker’s improved tracking capabilities in making triggering decisions using the tracking information at L1. This trigger is specifically designed to get a handle on the events with LLPs exhibiting

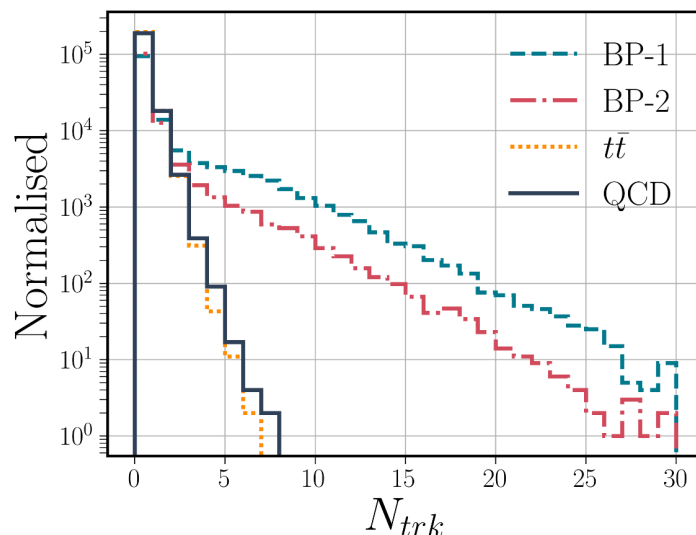


Figure 2. Comparison of displaced track multiplicity within $\Delta R < 0.3$ of jet for BP-1 (10 cm) and BP-2 (100 cm) LLP benchmarks, with $M_{\chi_1^0} = 800$ GeV and $M_{\chi_2^0} = 1600$ GeV, along with $t\bar{t}$ and QCD background for jets with $p_T > 40$ GeV and $|\eta| < 2.5$.

shorter decay lengths. The current analysis uses a track-based trigger influenced by the CMS Track- H_T trigger [125]. The Track- H_T trigger used in the current study selects events where at least one displaced jet is present, and it works by calculating H_T from track-based jets. To form track-based jets, we begin by grouping tracks with a p_T greater than 2 GeV within a $|\eta| < 2$ range. These tracks are then binned based on their closest approach to the beam line in the z -direction, z_0 , with a bin size of 6 cm. The z_0 bin is chosen based on the highest scalar sum of p_T of tracks. Subsequently, the tracks in the chosen z_0 bin are clustered into jets using the anti- k_t algorithm with a cone radius of $R = 0.3$ for each event. Jets with $p_T > 5$ GeV are considered for further analysis. Jets with at least two displaced tracks ($|d_0| > 1.5$ mm) as constituents are classified as displaced jets. For events that contain at least one displaced jet in the collection, H_T is calculated by summing the p_T of all the jets, including those classified as displaced. In our study, an event must have a track-based H_T threshold greater than 160 GeV to trigger, as inferred from [125].

- **Displaced Calo-Jet:** the upgraded ECAL at HL-LHC will provide precise timing information for ECAL energy deposits, with a timing resolution of approximately 30 ps for a 20 GeV energy deposit during the initial runs of HL-LHC [107]. However, it is important to note that timing resolution may degrade over time as more data is collected. To utilise this timing information at the L1 trigger level and trigger events with displaced jets, the CMS experiment has proposed an L1 trigger incorporating ECAL timing information. For the current analysis, we utilise the L1 trigger developed in [10] that uses ECAL timing information for identifying displaced jets.

For the trigger, energy deposits from ECAL and HCAL are clustered to form jets within the $|\eta| < 1.5$ region, utilising the anti- k_T algorithm with a cone size of $R = 0.3$.

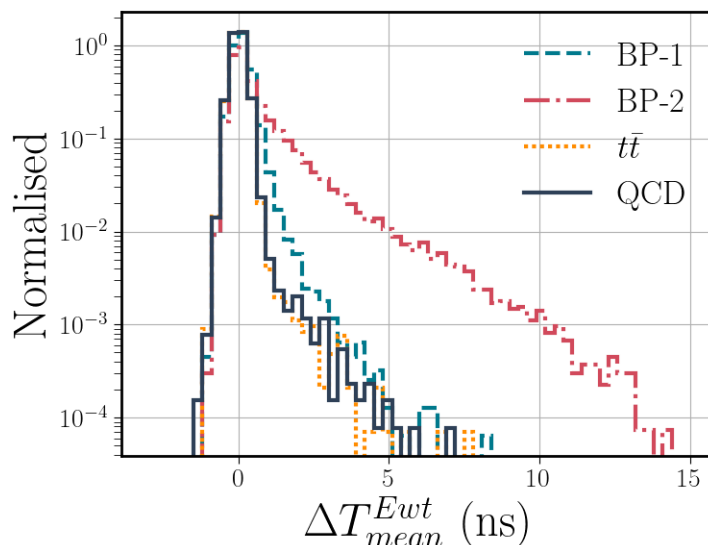


Figure 3. Energy weighted mean timing of jets for BP-1 and BP-2, with $M_{\chi_1^0} = 800$ GeV and $M_{\chi_2^0} = 1600$ GeV, along with $t\bar{t}$ and QCD background for jets with $p_T > 40$ GeV and $|\eta| < 1.5$.

Each ECAL tower is required to have an energy deposit of at least 0.5 GeV, while each HCAL tower needs an energy deposit of at least 1 GeV [106]. The clustering of jets is done using inputs from both ECAL and HCAL, but only the ECAL inputs are used to determine the timing of the jet. A jet is selected if at least one of the ECAL towers in its constituents has an energy deposit greater than 1 GeV [106]. Each ECAL tower’s timing is calibrated relative to the origin. The jet’s timing is determined using the energy-weighted average of the timings from the ECAL towers inside that jet. Figure 3 shows the energy-weighted mean timing of jets with $p_T > 40$ GeV and $|\eta| < 1.5$ for two LLP benchmark scenarios, BP-1 and BP-2, along with the two main background sources.

Figure 3 shows that LLPs in the benchmark scenario BP-2, characterised by longer decay lengths, exhibit higher timing values than BP-1 with shorter decay length. Furthermore, LLPs in BP-2 demonstrate significantly higher timing values than the background. For our current study, we select an event at L1 if it contains at least one jet with a timing value ($\Delta T_{\text{mean}}^{\text{Ewt}}$) greater than 1.2 ns, a jet transverse momentum (p_T^{jet}) greater than 35 GeV, and at least 4 ECAL towers in the jet. The threshold values used in our study are determined through explicit rate calculations as described in [10]. These calculations consider the background rate constraint for the specific scenario of 200 PU with the timing resolution at the integrated luminosity of 1000 fb^{-1} .

- **Single TkIsoElectron:** requires at least one prompt, an isolated electron from the primary vertex (PV) with p_T greater than 28 GeV, within $|\eta| < 2.4$. The isolation of each electron is computed by adding the p_T of all tracks within a cone of size $\Delta R < 0.3$, not including the p_T of the electron, divided by the sum of the p_T of all tracks within the same ΔR cone. Here, ΔR is computed as $\sqrt{\Delta\eta^2 + \Delta\phi^2}$, where $\Delta\phi$ and $\Delta\eta$ are the differences in azimuthal angle and pseudorapidity, respectively, between the electron and the tracks. For the current study, a fairly isolated electron is required, with an

L1 Trigger	Online thresholds	Rate (kHz)
Single TkIsoElectron	$p_T > 28.000 \text{ GeV}, \text{Iso} < 0.1$	28
Single TkIsoMuon	$p_T > 22.000 \text{ GeV}, \text{Iso} < 0.1$	12
Track- H_T	$H_T > 160.000 \text{ GeV}, p_T^{\text{jet}} > 5.000 \text{ GeV}$	20
Displaced Calo-jet	$\Delta T > 1.2 \text{ ns}, p_T^{\text{jet}} > 35.000 \text{ GeV}, N_{\text{tow}} \geq 4$	20

Table 2. Selection cuts for the L1 triggers as well as their respective rate limit at the HL-LHC as inferred from [106].

isolation factor (sum of p_T of tracks divided by sum of p_T of all tracks) less than 0.1. The trigger thresholds for our study are adopted from the L1 trigger menu designed for the HL-LHC, as outlined in reference [106].

- **Single TkIsoMuon:** requires at least one prompt, isolated muon with $p_T > 22 \text{ GeV}$ from PV, within $|\eta| < 2.4$. The isolation of each muon is calculated in the same way as explained above for the electron trigger, i.e., by summing the p_T of all tracks within a $\Delta R < 0.3$ cone around the muon, excluding the muon’s own p_T , divided by the sum of the p_T of all tracks within the same ΔR cone. Similarly, for this trigger, the muon isolation factor is required to be less than 0.1. The trigger thresholds used in our study are obtained from the L1 trigger menu for the HL-LHC as provided in reference [106].

Various thresholds for object p_T , isolation, H_T and jet timing for the above-mentioned L1 triggers, as well as the limits on the total allowed rate from a particular trigger, are summarised in table 2.

Figure 4 displays the variation of trigger efficiency with mean proper decay length for the triggers mentioned above, as well as the combined trigger efficiency for four different LLP scenarios. Although we only consider LLPs with masses higher than 500 GeV in the current analysis, trigger efficiency for LLPs with masses ranging from light ($M_{\chi_1^0} = 50 \text{ GeV}$) to very heavy ($M_{\chi_1^0} = 1400 \text{ GeV}$) is shown to depict the variation of trigger efficiency with mass of LLP. We also show the variation of trigger efficiency for one of the benchmark points with $M_{\chi_2^0}/M_{\chi_1^\pm} = 1600 \text{ GeV}$ and $M_{\chi_1^0} = 800 \text{ GeV}$. LLPs with decay lengths ranging from 1 cm to 500 cm and originating from the decay of χ_2^0/χ_1^\pm with masses varying from 250 GeV to 1600 GeV are considered. The observations obtained from figure 4 are summarized as follows:

- The displaced Calo-Jet trigger is particularly effective for LLPs with longer decay lengths, especially for heavier LLPs. This is because the trigger utilises timing information from the ECAL deposits, and LLPs that decay later in the detector will exhibit a more significant time delay. As the mass of the LLPs increases, the time delay also increases, as these heavier LLPs travel at a slower pace, resulting in a more considerable time delay.
- Furthermore, the track H_T trigger performs best for LLPs with smaller decay lengths, as the efficiency of extended track reconstruction degrades with increasing $c\tau$. The trigger efficiency is also reduced for LLP benchmarks with smaller mass differences between χ_2^0/χ_1^\pm and their decay products due to less hadronic activity in the calorimeter.

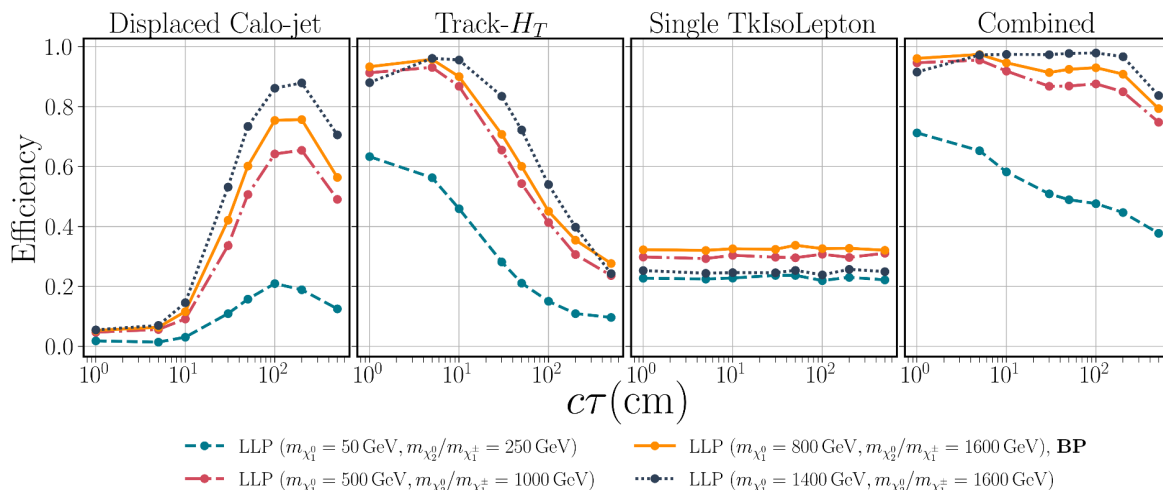


Figure 4. Variation of trigger efficiency for displaced Calo-Jet, Track- H_T , and single TkIsoLepton triggers with decay length for four LLP scenarios with one benchmark scenario (BP). The combined trigger efficiency is also shown.

- The lepton trigger efficiency remains unaffected by the $c\tau$ parameter, but it decreases as the mass degeneracy between the LLP and χ_2^0/χ^\pm increases, due to kinematic suppression. This implies that the efficiency of lepton triggers will be lower for benchmark points with smaller mass differences between the LLP and χ_2^0/χ^\pm .
- The combined trigger efficiency decreases with increasing $c\tau$ for every benchmark point, which can be explained by looking at the individual trigger efficiencies. The decrease in efficiency as the decay length increases is likely because LLP events with longer decay lengths have a higher chance of escaping the detection region before being triggered.
- Single TkIsoLepton triggers, along with the Track- H_T trigger and displaced Calo-Jet trigger, complement each other in selecting LLP events in both the lower and higher ends of the decay length spectrum for both lighter and heavier LLPs. This implies that combining these triggers can effectively select LLP events across a wide range of decay lengths and masses.

It is important to highlight the significance of displaced jet triggers in detecting LLP events, especially since lepton triggers are limited to selecting events with prompt leptons. In the current study, prompt leptons mainly come from the inclusive decay of W and Higgs bosons, which have relatively low branching fractions. For instance, in a scenario where the LLP originates from the decay of a 1000 GeV particle with a mass of 500 GeV and a decay length of 10 cm, the efficiency of the lepton trigger is approximately 30%. However, the overall efficiency increases significantly when displaced jet triggers are included. With a decay length of 10 cm, the efficiency rises to around 91%, and for a longer decay length of 100 cm, the efficiency remains high at 89%. This demonstrates that incorporating displaced jet triggers significantly enhances the efficiency of detecting LLPs with shorter as well as longer decay lengths. In LLP scenarios with shorter decay lengths, the track H_T trigger is more effective, while in contrast, the Calo-Jet trigger is more effective for events with longer decay lengths.

Sample	Single TkIsoLepton	Track- H_T	Displaced Calo-Jet	Combined
QCD	8.108	234.643	18.502	255.911
$t\bar{t}$	15.085	6.067	0.579	19.780
W+Jets	1.420	0.122	0.026	1.546
Total	24.613	240.831	19.106	277.237

Table 3. Background rate (in Hz) for the various background processes using Single TkIsoLepton, Track- H_T and Displaced Calo-Jet trigger. The combined rate is also shown for each sample, as well as the total rate for complete background.

In conclusion, the most effective approach to efficiently select LLP events with varying decay lengths, from very small to very large, is to use a combination of different L1 triggers.

Now, let's analyse the rate of background events that are identified by specific triggers to ensure compliance with the rate limits set by the CMS experiment [106]. The background trigger rate, measured in hertz (Hz), is given by,

$$\mathcal{R}_B = \sigma \times \mathcal{L} \times \epsilon_B \tag{3.1}$$

Here, σ is the background cross section in nanobarns (nb), \mathcal{L} is the peak instantaneous luminosity in nb^{-1}Hz , and ϵ_B represents the efficiency with which the triggers can detect a background event. At the HL-LHC, we anticipate a peak instantaneous luminosity (\mathcal{L}) of $5.6 \times 10^{34} \text{cm}^{-2}\text{s}^{-1}$, equivalent to $56 \text{nb}^{-1}\text{Hz}$ under a scenario with 140 PU.

The rates are computed using the leading-order cross sections from the PYTHIA simulation, and we should consider that higher-order corrections could potentially double these figures. Table 3 presents a breakdown of the background rates contributed by various triggers, as previously discussed, highlighting the most dominant background processes. As we can see from referring to tables 2 and 3, it is evident that the background event rate captured by the triggers used in this study is considerably below the maximum permitted bandwidth. The collective bandwidth for all triggers, as specified in the CERN report [106], is approximately 70 kHz. However, the background rate for this analysis is constrained to an impressively low rate of roughly 0.3 kHz. This demonstrates the high effectiveness of the triggers employed in this study for isolating relevant signal events and filtering out the background.

4 Offline analysis

After triggering the events at L1, the next step is to analyze the selected events offline to remove the background events that have large cross-sections. We have divided the offline analysis of events selected at L1 using triggers, as defined in section 3, into three separate and independent parts. Here, we utilize information from various sub-detectors of the CMS experiment to efficiently select signal events containing LLPs with a wide spectrum of decay lengths (1 cm to 500 cm). As we have seen from figure 4, while the track-based trigger performs well for LLPs with shorter decay lengths, timing information is efficient for triggering LLPs with longer decay lengths. We follow the same strategy here, using tracking information to focus on LLPs with shorter decay and timing information from ECAL and MTD for

LLPs with larger decay lengths. We divide the offline analysis into three separate and independent parts, as described below,

- **Cut-based analysis (CBA)**: to handle LLP scenarios with shorter decay lengths, we use tracking information and adopt a cut-based approach. This method efficiently selects signal events while significantly rejecting background contributions.
- **Multi-variate analysis-1 (MVA-1)**: for events with significant lifetimes, we perform a machine learning-based multivariate analysis, denoted MVA-1, independently on the jets from the events selected at L1. This analysis uses information from the MTD and associated data from the tracker as calculated previously.
- **Multi-variate analysis-2 (MVA-2)**: similar to MVA-1, we conduct a separate multivariate analysis, referred to as MVA-2, on the jets from the events selected at L1. This analysis targets LLP scenarios with large lifetimes, utilizing variables constructed with information from the ECAL and associated tracker data.

Dividing the analysis into three independent parts, with CBA focused on LLPs with smaller decay lengths and MVA-1 and MVA-2 on LLPs with larger decay lengths, helps us address the challenges associated with background suppression and signal extraction across a wide range of decay lengths. Utilizing these three approaches ensures the analysis remains sensitive to various LLP scenarios with a spectrum of decay lengths.

The final signal significance for each LLP benchmark point is calculated by combining results from the above approaches after removing duplicate events. In the following sections, we will provide a detailed explanation of the analysis approaches mentioned above.

4.1 Cut Based Analysis (CBA)

We begin by reconstructing the secondary displaced vertex, a key characteristic of the decay of LLPs, for the selected events using the set of displaced tracks. In our analysis, we reconstruct tracks taking into consideration the track reconstruction efficiency, which varies with the transverse displacement of tracks from the beam-line as achievable at Phase-I of the LHC for CMS [126] since no specific information about the track reconstruction efficiency is available for Phase-II. However, we assume that offline track reconstruction in terms of transverse displacement from the beam-line will remain the same for Phase-II as in Phase-I. Nevertheless, updated information will be needed to confirm this assumption. We form displaced vertices by clustering displaced tracks with transverse impact parameter $|d_0| > 1.5$ mm based on their spatial position. We identify vertices with at least two displaced tracks associated with the vertex. These criteria effectively filter out a significant number of prompt tracks associated with background processes, making secondary vertex reconstruction computationally manageable, especially for background processes predominantly dominated by QCD multi-jet events. Next, each vertex is assigned a unique ID and stored for further analysis.

Next, we compute two physics variables related to each selected displaced vertex,

- $N_{\text{trk}}^{\text{disp}}$ — The number of displaced tracks associated with the secondary vertex.
- M_{DV} — The invariant mass of the displaced secondary vertex, which is calculated using the displaced tracks that are associated with it.

In figure 5, we show the two-dimensional distribution of displaced track multiplicity ($N_{\text{trk}}^{\text{disp}}$) and invariant mass of the displaced vertex (M_{DV}). The distributions are shown for two LLP benchmark points, BP-1 and BP-2, as well as for the QCD and $t\bar{t}$ background. To ensure proper normalization of the data, each bin in the distribution is re-weighted such that the sum of the fraction of entries falling in every bin equals unity.

As shown in figure 5, the LLP benchmarks exhibit a significantly higher number of displaced tracks associated with the displaced vertex as the invariant mass of the displaced vertex increases compared to the backgrounds. This indicates that applying a suitable 2-dimensional cut on the displaced track multiplicity and the invariant mass of the displaced vertex can effectively reduce the contribution from the background events. In addition to mitigating the background events from QCD and $t\bar{t}$, implementing a higher threshold cut on both $N_{\text{trk}}^{\text{disp}}$ and M_{DV} can effectively remove the displaced vertices originating from the instrumental background as shown in [30, 34, 58]. This is because the displaced vertices from the instrumental background are typically collimated and have lower multiplicity and smaller invariant mass than the signal. As shown in [58], the instrumental background can be effectively mitigated by the requirement on M_{DV} and $N_{\text{trk}}^{\text{disp}}$ where they implement a threshold of 10 GeV on M_{DV} and a threshold of 5 for $N_{\text{trk}}^{\text{disp}}$ in the signal region. For the signal, the invariant mass of the displaced vertex is expected to peak around the mass of the LLP, which in this case is 800 GeV. However, it is essential to note that the number of reconstructed displaced tracks may be reduced for very short (≈ 1 cm) or very long decay lengths (≈ 500 cm), which can impact signal efficiency.

Owing to the inclusion of events from displaced Calo-Jet and track- H_T trigger at L1, the significant contribution to the background will originate from the jets coming from instrumental effects, the QCD processes and $t\bar{t}$ events. Contribution from these background sources can be significantly reduced by requiring events with high H_T where we calculate H_T by summing over the p_T of all the jets in each event. Furthermore, as previously stated, an appropriate two-dimensional threshold cut on M_{DV} and $N_{\text{trk}}^{\text{disp}}$ will also lead to a significant reduction in the background events. For the cut-based analysis, we apply the following selection cuts:

- **Event H_T** : we require events selected at L1 to possess event H_T greater than 500 GeV where H_T is calculated using jets with jet $p_T > 40$ GeV.
- **$N_{\text{trk}}^{\text{disp}}$** : we require at least one reconstructed secondary vertex with at least six associated displaced tracks, each with a transverse impact parameter ($|d_0|$) greater than 1.5 mm.
- **M_{DV}** : we require the invariant mass of the reconstructed secondary vertex to be greater than 20 GeV.

Events selected after imposing the abovementioned cuts are sorted and stored for further analysis, where we combine results from MVA-1 and MVA-2 with CBA. Now, let us discuss the second and third approaches, MVA-1 and MVA-2.

4.2 Multi Variate Analysis-1 (MVA-1)

Now, we turn our attention to the utilisation of MTD timing information in the current analysis. At the HL-LHC, MTD will be positioned between the tracker and the electromagnetic

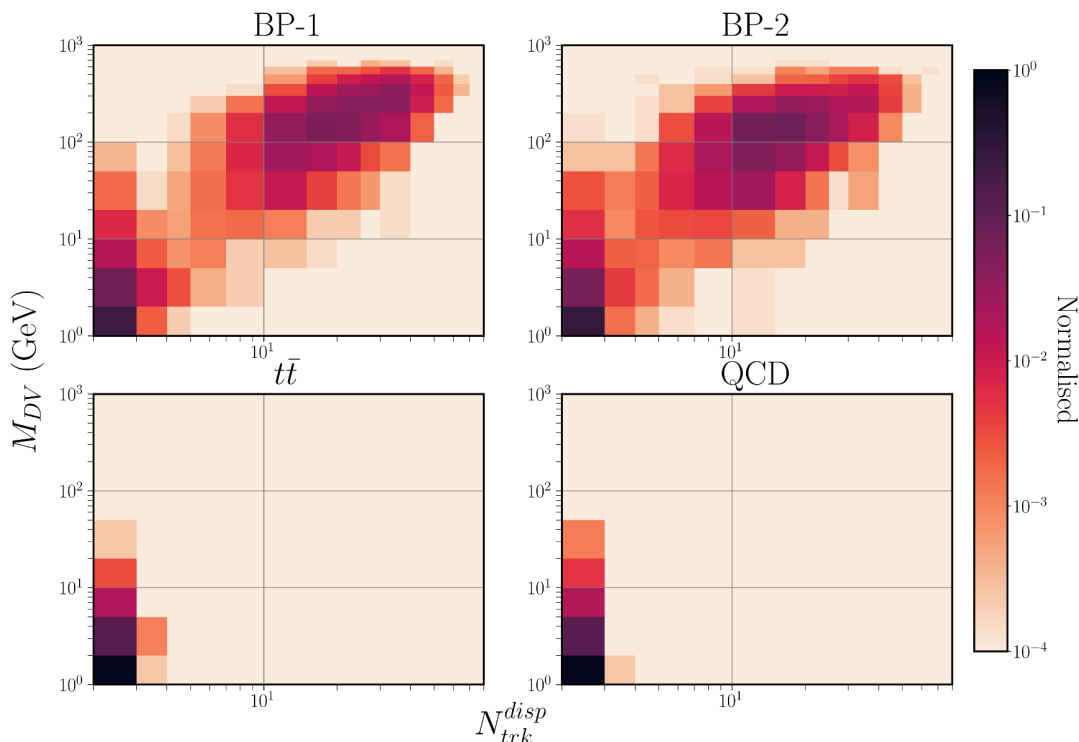


Figure 5. Two-dimensional distribution showing the relationship between the number of displaced tracks ($N_{\text{trk}}^{\text{disp}}$) and the displaced vertex invariant mass (M_{DV}) for the two LLP benchmarks, BP-1 and BP-2, along with the $t\bar{t}$ and QCD background.

calorimeter of the CMS detector, providing precise timing information for the charged particles originating within the tracker. Currently, precision timing information from the MTD is proposed to be included for the offline analysis in the CMS detector instead of the online trigger system. Including the partial readout of the MTD for a region of interest at L1 is a possibility in the future upgrades of the HL-LHC [108]. However, in this work, we have mainly focused on including output from MTD in the offline analysis, where we can construct complex physics variables out of the output from various sub-detectors, including MTD. At HL-LHC, the primary objective of the MTD will be to help mitigate the effect of the huge amount of PU on physics analysis and restore the physics performance at par with Phase-I of LHC. However, the role of MTD will be pivotal in studying exotic particles such as LLPs, where the decay of the particles is delayed, and timing information from the MTD can be efficiently used to search for such particles.

Timing information can be extracted from the MTD with the timing resolution of 30 ps for MTD hits from the charged particles with $p_T > 0.7$ GeV in the barrel region ($|\eta| < 1.5$) and $p > 0.7$ GeV in the endcap region ($1.5 < |\eta| < 3.0$). Excellent coverage and timing resolution of the MTD can be leveraged to construct the timing variables for the jets originating due to the decay of LLPs, which will be delayed in time. MTD layer is proposed to be placed at the radius of 1.16 m between the tracker and barrel ECAL, which is placed at the radius of 1.29 m.

In order to construct timing variables for jets using information from MTD, we will require MTD hits directly below the clustered jets within the specific cone along the jet

axis. In addition to MTD hits coming from tracks, whether displaced or prompt, we have two additional lists of MTD hits — one where MTD hits originate from reconstructed displaced tracks with $|d_0| > 1.5$ mm and the second one where we have MTD hits with no reconstructed tracks associated with the hits. We construct physics variables using the three above-mentioned collections of MTD hits. We consider MTD hits only within a narrow cone radius directly below the jets to reduce the PU contamination. For MTD hits associated with tracks, we only consider tracks with $p_T > 2$ GeV and can be reconstructed using the track construction efficiency as explained before. We have constructed the following timing variables using the above-mentioned three MTD hits collection directly below a clustered jet in a cone with $\Delta R < 0.3$ and axis matching with the jet axis:

- \mathbf{N}_{MTD} : the number of MTD hits with associated reconstructed tracks within $R = 0.3$ of the jet axis. Hard signal jets will contain a comparatively higher number of MTD hits when compared to the background. LLPs decaying after the MTD and before the ECAL and HCAL boundary will have energy deposition in the calorimeters but with no associated MTD hits. So, MTD hit multiplicity will decrease with the increase in the decay length; however, distribution will mainly be dominated by the charged PU hits.
- $\mathbf{N}_{\text{MTD}}^{\text{disp}}$: the number of MTD hits with associated reconstructed tracks within $R = 0.3$ of the jet axis with $|d_0| > 1.5$ mm. Displaced jets will contain a comparatively higher number of MTD hits coming from displaced tracks when compared to the background. MTD hit multiplicity will decrease with the increase in the decay length.
- $\mathbf{N}_{\text{MTD}}^{\text{NT}}$: the number of MTD hits within $R = 0.3$ of the jet axis with no associated tracks. Track reconstruction efficiency follows an efficiency curve where the efficiency of reconstructing a track will degrade with the transverse distance (D_{xy}) from the beam line. As a result, we will have a higher number of MTD hits with no associated tracks for displaced LLPs. However, this number will decrease with the decreasing decay length as we will have more and more tracks with smaller D_{xy} being reconstructed. In contrast, for prompt processes, most of the MTD hits will have associated tracks; hence, $N_{\text{MTD}}^{\text{NT}}$ will be less than displaced LLPs.
- \mathbf{T}_{raw} : the mean of the timing of MTD hits constituting a jet within cone radius of $R = 0.3$. To compute T_{raw} , no timing calibration corresponding to the position of MTD hits has been applied. For highly displaced LLPs, T_{raw} will have higher values compared to prompt processes, but since the majority of MTD hits inside a jet will be coming from PU interactions, T_{raw} measurement will mainly be dominated by the timing of PU hits. Also, the timing of the jet will depend on the position and p_T of the jets. Jets with low p_T depositing energy at higher η values away from the central part of the barrel will have higher timing, which is valid for both LLPs and the prompt background processes.
- $\mathbf{T}_{\text{raw}}^{\text{disp}}$: the mean of the timing of MTD hits associated with displaced tracks constituting a jet within a cone radius of $R = 0.3$. For highly displaced LLPs, T_{raw} will have higher values compared to prompt processes where displaced track multiplicity is very low.

- $\mathbf{T}_{\text{raw}}^{\text{NT}}$: the mean of the timing of MTD hits with no associated tracks within the cone radius of $R = 0.3$ of the jet axis. As we discussed earlier, most tracks can be successfully reconstructed for prompt processes and LLPs with very short decay lengths; therefore, jets from such processes are less likely to leave MTD hits with no reconstructed tracks. In such cases, $T_{\text{raw}}^{\text{NT}}$ will be zero when no MTD hit is found with no reconstructed tracks. However, with the increase in decay length, we will have more and more number of MTD hits with no reconstructed tracks. Furthermore, for prompt processes, contribution to the tail of the timing distribution of the jet will be coming from the hits with very low p_T tracks, which did not get reconstructed.
- $\mathbf{T}_{\text{calib}}$: the mean of the timing of the MTD hits within $R = 0.3$ of the jet axis calibrated with respect to origin $(0,0,0)$. Calibration of the temporal position of each hit is done to mitigate the effect of the position of the MTD hit in the $\eta - \phi$ plane on the timing of the MTD hit. The timing of each MTD hit is corrected such that if the particle travels with the speed of light from the origin to the position of the MTD hit, it should take zero seconds to reach there. Hence, the timing of the delayed particles will be given as the difference between the raw timing of the hit, as discussed before, and the time taken by a massless particle travelling with the speed of light originating from the origin to reach the position of the MTD hit. T_{calib} will have higher values and longer tail in the timing distribution for displaced jets than those coming from prompt processes.
- $\mathbf{T}_{\text{calib}}^{\text{disp}}$: the mean of the timing of the MTD hits associated with displaced tracks as explained above within $R = 0.3$ of the jet axis calibrated with respect to origin $(0,0,0)$. T_{calib} will have higher values and longer tail in the timing distribution for displaced jets compared to jets coming from prompt processes where displaced track multiplicity will be very low compared to displaced processes.
- $\mathbf{T}_{\text{calib}}^{\text{NT}}$: the mean of the calibrated timing of the MTD hits with no associated tracks within $R = 0.3$ of the jet axis. As explained earlier, prompt processes and displaced particles with very small decay lengths will have MTD hits, which can be easily associated with the reconstructed tracks. More and more number of MTD hits will be available for highly displaced particles with no reconstructed tracks to be fed into the calculation of T_{calib} . As a result, the timing distribution of the displaced jets will have slightly higher values of T_{calib} when compared to prompt processes. However, T_{calib} will have smaller values as we consider LLPs with shorter and shorter decay lengths. For prompt processes, contribution to the tail of the timing distribution of the jet will be coming from the hits with very low p_T tracks which did not get reconstructed.
- $\mathbf{p}_T^{\text{Ratio}}$: the Ratio of the sum of p_T of reconstructed tracks (prompt as well as displaced) associated with MTD hits within $R = 0.3$ of the jet and the corresponding jet p_T . For LLPs with large decay lengths, fewer and fewer prompt tracks will be reconstructed, and hence, the number of MTD hits with no associated tracks will be smaller. As a result, there will be a more significant mismatch between actual jet p_T and p_T calculated using tracks with associated hits. This effect will be minimal for prompt processes where most MTD hits will have associated tracks.

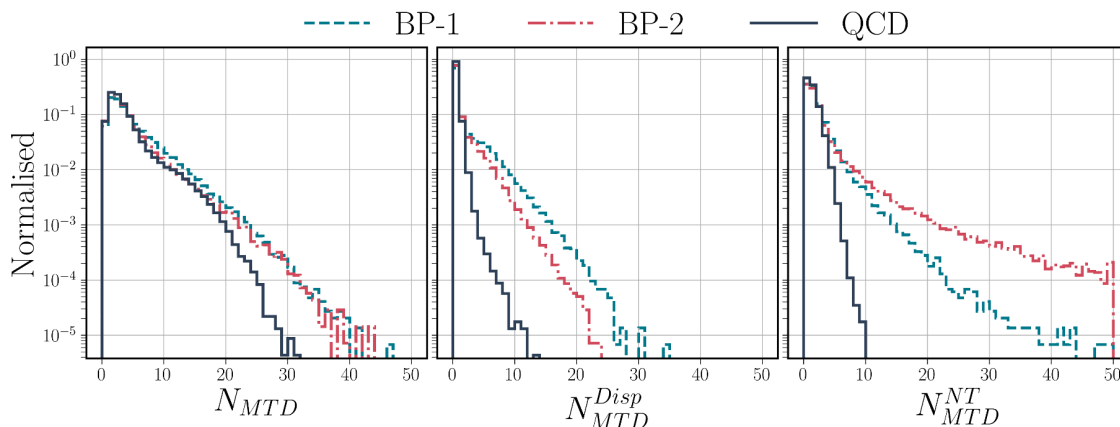


Figure 6. Distribution of the Multiplicity of MTD (N_{MTD}) hits for three MTD hits collections, for the QCD background, and the two LLP benchmark points BP-1 and BP-2, at the HL-LHC.

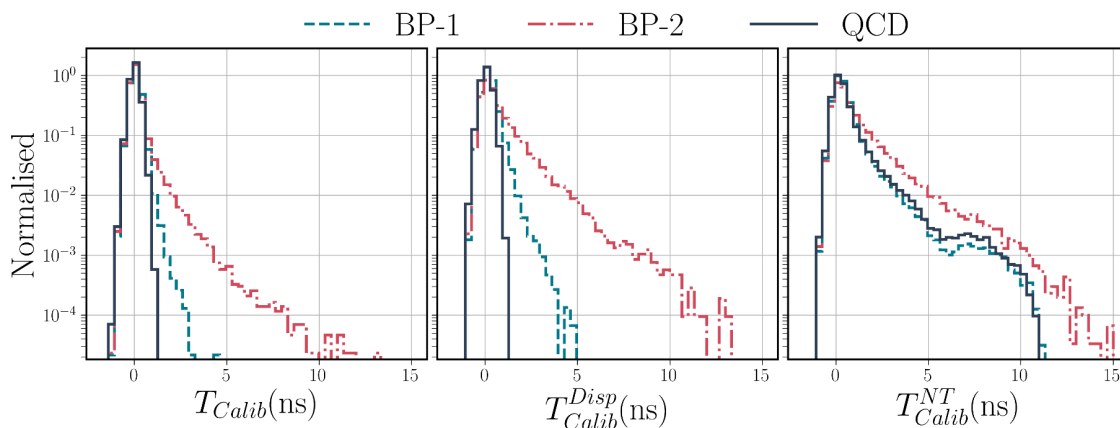


Figure 7. Calibrated time (T_{calib}) calculated using three MTD hits collections for the QCD background and the two LLP benchmark points, BP-1 and BP-2, at the HL-LHC.

- D_T^{Med} : the median of the transverse distance calculated using the reconstructed tracks that have hits in the MTD and are associated with the jets within $\Delta R < 0.3$.

Figure 6 shows the multiplicity of MTD hits for each jet, as measured using three lists of MTD hits for LLP benchmarks BP-1 and BP-2 and the QCD background under the conditions of HL-LHC. Similarly, figure 7 and figure 8 depict the T_{calib} and T_{raw} , respectively, calculated using the three MTD hits collections.

From figure 6, 7, 8 and 9, We observe-

- LLP with a smaller decay length has more number of MTD hits compared to LLP with a higher decay length. LLPs, in general, have more number of MTD hits compared to background sources.
- The number of MTD hits with associated displaced tracks decreases with increasing LLP decay length, while for background, the number is significantly lower due to the absence of displaced tracks inside the jet.

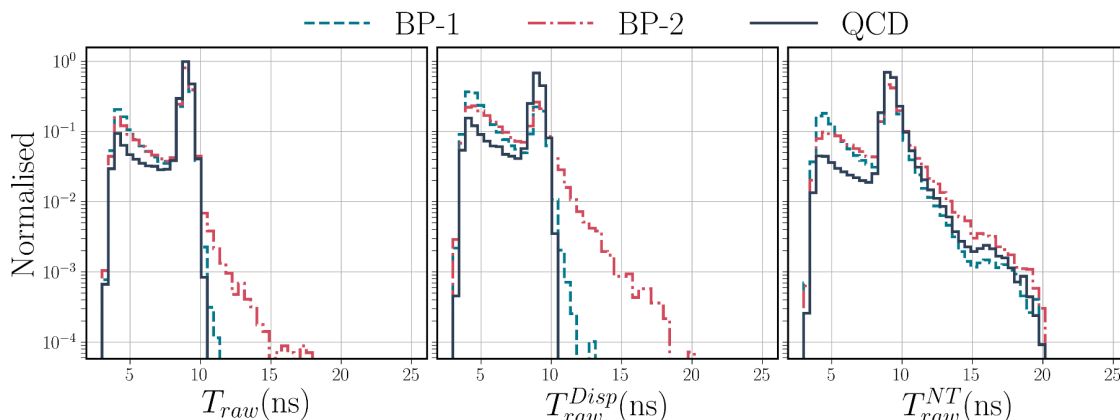


Figure 8. Raw time (T_{raw}) calculated using three MTD hits collections for the QCD background and the two LLP benchmark points, BP-1 and BP-2, at the HL-LHC.

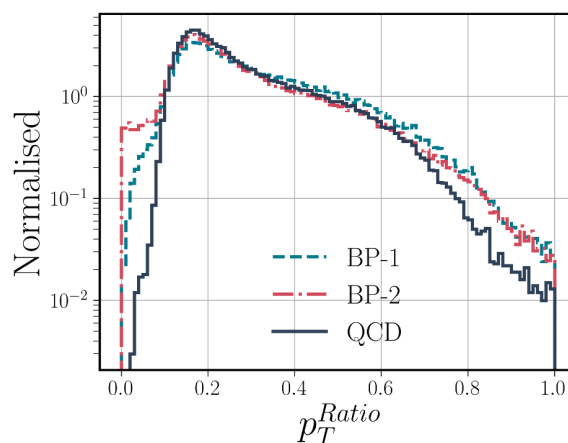


Figure 9. Ratio of the sum of p_T of tracks associated with MTD hits within $\Delta R < 0.3$ of the calorimeter jet and jet p_T , as calculated using calorimeter inputs using the anti- k_T jet algorithm with $R=0.3$, for the QCD background, and the two LLP benchmark points BP-1 and BP-2, at the HL-LHC.

- LLP with higher decay length have more number of hits with no associated tracks compared to LLP with lower decay length while backgrounds have very less number of MTD hits with associated tracks since most of the hits in MTD will be coming from promptly produced particles.
- Tail of the timing distribution (T_{calib} and T_{raw}) calculated using MTD hits with associated tracks and MTD hits associated with displaced tracks only increases with decay length for LLPs and background and signal can be easily distinguished.
- Timing calculated using MTD hits with no associated tracks has a longer tail for LLP with higher decay lengths. High timing in timing distribution calculated using MTD hits with no associated tracks in the background is associated with low p_T PU tracks, which move very slowly and contaminate the jet timing.

- Tail at the lower end of the p_T^{ratio} is observed for LLPs because of the mismatch between jet p_T and p_T calculated using tracks associated with MTD hits. The effect is more pronounced for higher decay lengths because of the higher probability of not finding hits with associated tracks.

In MVA-1, we utilise an XGBoost (Extreme Gradient Boosting) [127] model trained on physics variables constructed using MTD information to specifically target LLPs with longer lifetimes. XGBoost works by iteratively building a series of decision trees, where each tree corrects the errors made by the previous trees. To minimise the loss function, which measures the difference between the predicted and actual values, XGBoost uses a gradient descent optimisation algorithm. In our analysis, we use the following set of XGBoost parameters to train our model for multi-class classification:

- **objective:** the objective of our model was to perform multi-class classification using the ‘multi:softprob’ approach, which computes the predicted probabilities for each class.
- **num_class:** this parameter was set to 8, indicating the total number of classes in our multi-class classification problem with class 0 representing the signal while other 7 classes ranging from 1 to 5 representing QCD background in different H_T^{gen} bins while class 6 and 7 representing $t\bar{t}$ and W+Jets background respectively.
- **eval_metric:** we used ‘mlogloss’ as our evaluation metric, which calculates the multi-class logarithmic loss during the training process. It provides a measure of the model’s performance.
- **learning_rate:** we utilised a learning rate of 0.1, which determines the step size at each boosting iteration.
- **early_stopping_rounds:** we implemented early stopping with a value of 5 for this parameter. This means that if the loss does not decrease further after 5 consecutive iterations, the training process is halted. The purpose of early stopping is to prevent over-training and improve the generalisation ability of the model.
- **colsample_bytree:** this parameter was set to 0.3, indicating the fraction of columns to be randomly sampled for each tree during training.
- **max_depth:** we set the maximum depth of each tree in our model to 6. This restricts the depth of the individual trees, preventing overfitting and improving generalisation.
- **alpha:** the alpha parameter was assigned a value of 4, which controls the L1 regularisation term on the weights. It helps reduce the complexity of the model and prevents overfitting.
- **tree_method:** the ‘tree_method’ parameter was set to ‘gpu_hist’, indicating the use of GPU acceleration for training the model.
- **num_boost_rounds:** to ensure convergence of the training and achieve the minimum loss, we set the number of boosting rounds to 1000 epochs. This value determined the maximum number of iterations performed during the training process.

The XGBoost model is trained using a set of variables as described previously and tabulated in the third column of table 4. We focus on LLP benchmark points with $M_{\chi_2^0}/M_{\chi_1^\pm} = 1600$ GeV and vary the mass of the LLP, $M_{\chi_1^0}$, from 500 GeV to 1000 GeV.

Events selected at L1 utilising displaced and lepton triggers are further required to have offline event H_T greater than 500 GeV where event H_T is calculated in a similar manner as for CBA as explained in section 4.1. Only 6 leading jets per event with transverse momentum greater than 100 GeV are considered in the training process to exclude most pileup jets and only keep the jets coming from the hard interaction. The decay length of the LLPs in our benchmark scenarios ranges from 1 cm to 500 cm. To account for different decay lengths, we train three separate XGBoost models, each targeting a specific range of decay lengths.

Three models are trained using LLP benchmark scenarios exhibiting decay lengths of 1 cm, 50 cm and 200 cm to target LLPs with decay lengths in the range of 1 cm to 5 cm, 10 cm to 50 cm and 100 cm to 500 cm, respectively. We choose the mass of the LLP, $M_{\chi_1^0} = 800$ GeV for training the XGBoost models for each decay length, as it falls within the moderate range of LLP masses considered in our analysis, with $M_{\chi_2^0}/M_{\chi_1^\pm}$ fixed at 1600 GeV. Each jet in the training sample for the background is assigned a weight according to process cross-section and the number of generated events for that particular sample such that the sum of weights is unity. Signal jets are assigned unit weights. The trained XGBoost models are then utilised to classify LLPs in the respective decay length ranges in the subsequent analysis steps.

We divide the jets selected at L1 and after the pre-selection cuts, as defined above, into training and testing datasets of equal size. We have approximately 3600k jets from $t\bar{t}$ events and 2200k jets from QCD dijet events, the two dominant background sources. For signal benchmark points with decay lengths of 1 cm, 50 cm, and 200 cm, we have approximately 5800k, 5400k, and 4600k jets, respectively.

To highlight the significance of timing information in selecting LLP events with large lifetime, we show the feature importance of three crucial variables for the MTD in three different LLP scenarios, with decay lengths of 1 cm, 50 cm, and 200 cm in figure 10 (*left*). Feature importance is evaluated using the gain metric, which quantifies the improvement in accuracy achieved by a feature in the decision tree branches. In the case of MTD, timing information is derived from tracks (displaced or prompt) that leave hits in the MTD or from hits with no associated tracks. As shown in figure 10 (*left*), Jet timing calculated using MTD hits with associated tracks performs well for LLP scenarios where the decay length allows for the reconstruction of a larger number of tracks, including displaced ones. However, for LLPs with very long decay lengths, the timing of jets calculated using MTD hits with no associated tracks gains more significance due to the abundance of MTD hits without associated tracks.

In figure 10 (*right*), we present the signal efficiency versus background rejection in terms of Receiver Operating Characteristic (ROC) curves for three different decay lengths, namely 1 cm, 50 cm, and 200 cm, for LLPs with $M_{\chi_2^0} = 1600$ GeV and $M_{\chi_1^0} = 800$ GeV. The plots demonstrate that the MVA-1 approach, which incorporates timing information from the MTD, exhibits significantly improved performance for LLP scenarios with longer decay lengths compared to those with shorter decay lengths while maintaining good performance for LLP scenarios with shorter decay lengths. This improvement can be attributed to the inclusion of timing information from MTD, which aids in better discriminating between signal and background events, particularly for LLPs with longer decay lengths.

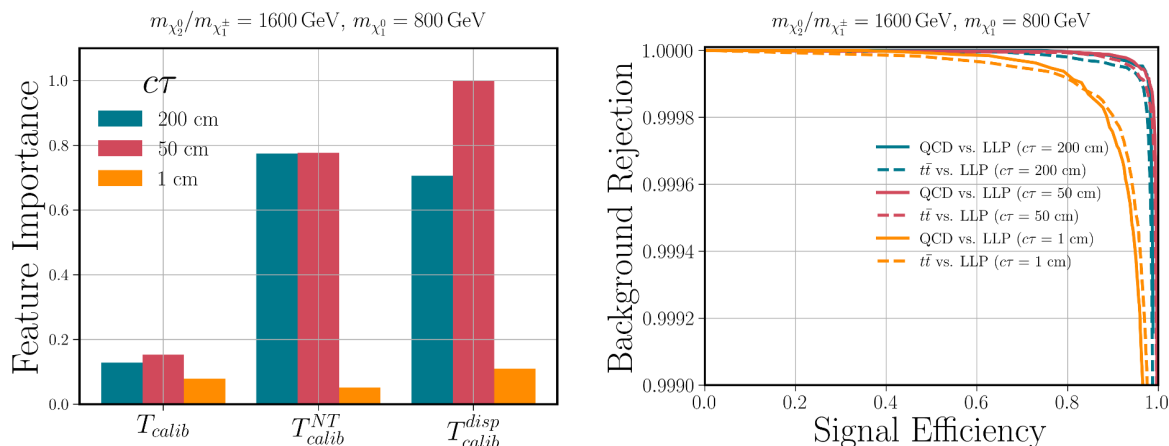


Figure 10. Relative feature importance of three important variables of MVA-1 for three LLP scenarios where decay length is 1 cm, 50 cm and 200 cm (*left*) and classification in terms ROC for two dominant background (QCD and $t\bar{t}$) for LLP with decay length 1 cm, 50 cm and 200 cm (*right*).

To finalise the event selection, we impose the prerequisite of at least one jet in every event that exhibits a very high signal probability. This signal probability is determined based on the amount of background rejection required, which will depend on the decay length of the LLP on which the model was trained.

4.3 Multi Variate Analysis-2 (MVA-2)

Now, we will shift our attention to the timing of ECAL tower constituents within jets to construct various timing variables for jets. For jet formation, we require ECAL and HCAL towers with energy deposits $E_{em} > 0.5 \text{ GeV}$ and $E_{had} > 1 \text{ GeV}$, respectively. Timing is calculated only for those jets with at least one ECAL tower exceeding an energy deposit of 1 GeV. For timing calculation, we only take into account ECAL towers by requiring $E_{had} < 0.0001 \text{ GeV}$ and $E_{em} > 0.5 \text{ GeV}$. In section 3, we have already utilized one of the timing variables, namely the energy-weighted mean timing of the jet ($\Delta T_{\text{mean}}^{Ewt}$), which is used in the design of the L1 trigger based on ECAL timing. Additionally, we have computed several other measures for the jets using the ECAL timing. These measures are listed as follows:

- ΔT_{mean} : the average timing of all ECAL crystals associated with the jet as shown in equation (4.1). Here, i refers to all ECAL crystals within the jet, and N is the complete count of the crystals associated with the jet.

$$\Delta T_{\text{mean}} = \frac{\sum \Delta T_i}{N}, \tag{4.1}$$

- ΔT_{median} : the median timing of all ECAL crystals associated with the jet.
- ΔT_{RMS} : the root mean square value of the timing of all ECAL crystals within the jet as computed in equation (4.2).

$$\Delta T_{\text{RMS}} = \sqrt{\frac{\sum \Delta T_i^2}{N}}, \tag{4.2}$$

- $\sum \Delta T$: the sum of the timing of all ECAL crystals in the jet.
- $\Delta T_{\text{mean}}^{\text{Ewt}}$: the energy-weighted mean timing of all ECAL crystals in the jet. This is computed as the sum of the product of each crystal's timing and energy divided by the total energy of all crystals within the jet, as in equation (4.3).

$$\Delta T_{\text{mean}}^{\text{Ewt}} = \frac{\sum \Delta T_i \times E_i}{\sum E_i} \quad (4.3)$$

- $\Delta T_{\text{mean}}^{\text{ETwt}}$: the transverse energy-weighted mean timing of all ECAL crystals in the jet as shown in equation (4.4).

$$\Delta T_{\text{mean}}^{\text{ETwt}} = \frac{\sum \Delta T_i \times E_{T,i}}{\sum E_{T,i}} \quad (4.4)$$

Before re-weighting with energy or transverse energy for the aforementioned timing variables, we adjust the timing of each ECAL crystal relative to the origin, as explained in section 3.

We have also implemented two more different calibration techniques for the above-mentioned timing variables, where we calibrate the timing of each crystal in the jet with respect to the primary vertex (PV) and the jet vertex (JV). The PV is determined by using prompt track collection. The vertex with the highest $\sum p_T^2$ is selected as the PV. Similarly, the JV is determined by considering all prompt tracks associated with the jet, located within a distance of $\Delta R < 0.3$ from the jet axis at the ECAL. The vertex with the maximum $\sum p_T^2$ is chosen as the JV.

Additionally, the mean timing of a jet is computed using only five or ten crystals, with the maximum time delay determined by multiplying the maximum value of time delay with the energy of the crystal, denoted as $(\Delta T \times E)_{\text{mean}}^{\text{Max5}}$, $(\Delta T \times E)_{\text{mean}}^{\text{Max10}}$. The mean timing of the jet calculated using 5 and 10 most energetic crystals is denoted as $\Delta T_{\text{mean}}^{\text{Max5}}$ and $\Delta T_{\text{mean}}^{\text{Max10}}$, respectively. We additionally compute two quantities, namely $(\Delta T \times E)_{\text{mean}}^{\text{TMax5}}$ and $(\Delta T \times E)_{\text{mean}}^{\text{EMax5}}$ where we calculate mean timing of a jet using only five ECAL towers, using the maximum value of time delay multiplied by the energy of the crystals, and this product is divided by the timing and energy of the five ECAL towers possessing highest energy and timing values respectively.

For quantities calculated above, If the jet contains less than five or ten towers, the values of $\Delta T_{\text{mean}}^{\text{Max5}}$ and $\Delta T_{\text{mean}}^{\text{Max10}}$ are assigned the same values as ΔT_{mean} , while the values of $(\Delta T \times E)_{\text{mean}}^{\text{Max5}}$ and $(\Delta T \times E)_{\text{mean}}^{\text{Max10}}$ as well as $(\Delta T \times E)_{\text{mean}}^{\text{TMax5}}$ and $(\Delta T \times E)_{\text{mean}}^{\text{EMax5}}$ are assigned the same values as $\Delta T_{\text{mean}}^{\text{Ewt}}$. Introducing such variables in the analysis is crucial as they are more resistant to PU contamination. Additionally, using crystals with the highest $\Delta T \times E$ values makes sure that PU hits with low energy and high ECAL timing do not significantly affect these variables.

We also compute several other quantities using information about the tracks and calorimeter towers associated with the jet-

- $\mathbf{p}_T^{\text{Ratio}}$ - Sum of the p_T of all tracks associated with the jet within a distance of $\Delta R < 0.3$ from the jet axis, divided by the jet p_T as determined through calorimeter inputs using the anti- k_T jet algorithm with $R=0.3$.

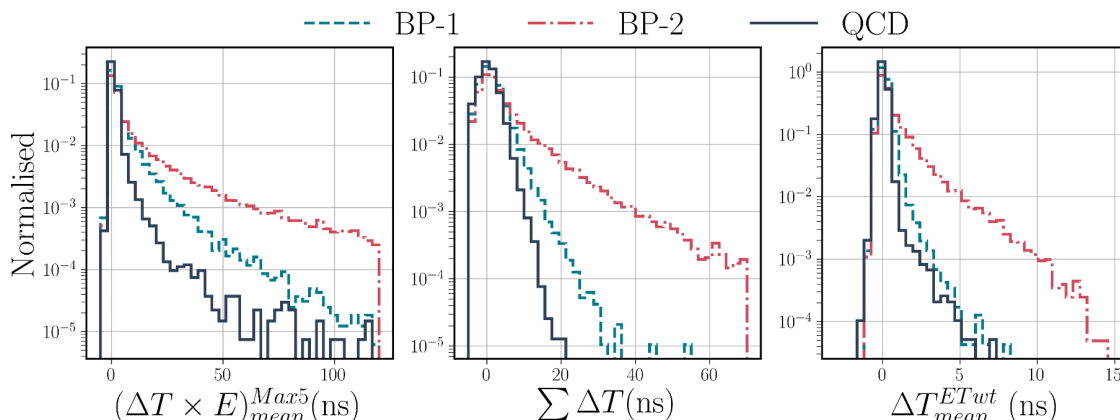


Figure 11. Energy-weighted mean timing of a jet, calculated exclusively from the 5 crystals having the maximum time delay, $(\Delta T \times E)_{\text{mean}}^{\text{Max5}}$ (left), sum of the timing all ECAL crystals associated with a jet, $\sum \Delta T$ (middle), and the transverse energy-weighted mean timing of the jet $\Delta T_{\text{mean}}^{\text{ETwt}}$ (right) for QCD background, and the two LLP benchmark points BP-1 and BP-2, at the HL-LHC.

- $\Delta\eta, \Delta\phi$ — Differences in the (η, ϕ) position of a jet as calculated using tracks and ECAL towers within the jet. (η, ϕ) of the jet using tracks is calculated by using p_T weighted mean of (η, ϕ) of tracks contained within $\Delta R < 0.3$ of the jet. Similarly, (η, ϕ) of the jet is calculated using the position of ECAL crystals contained within the jet by re-weighting them with crystal E_T . For displaced LLPs, the position of jets constructed using available tracks will differ from the position of the jets constructed using ECAL crystals since fewer and fewer displaced tracks will be reconstructed with the increase in the decay length of the LLPs.
- $\sum \mathbf{E}_{\text{tow}}$ — Sum of energy of ECAL towers within $\Delta R = 0.3$
- $\frac{\mathbf{E}_{\text{had}}}{\mathbf{E}_{\text{jet}}}$ — Fraction of energy deposited in hadron calorimeter (HCAL) compared to total jet energy.
- $N_{\text{trk,prompt}}^{\text{jet}}$ — Number of prompt tracks associated with jet located within a ΔR of less than 0.3 from the jet axis.
- $N_{\text{trk,disp}}^{\text{jet}}$ — Number of displaced tracks with $|d_0| > 1.5$ mm associated with jet within $\Delta R < 0.3$ of jet axis.

In figure 11, we show the distributions of three important timing variables constructed using the information from ECAL, namely $(\Delta T \times E)_{\text{mean}}^{\text{Max5}}$, $\sum \Delta T$, and $\Delta T_{\text{mean}}^{\text{ETwt}}$, for QCD background and two LLP benchmark points, BP-1 and BP-2.

As we can see from figure 11, LLP benchmarks exhibit a longer tail in the timing distribution when compared to the QCD background, as expected. Compared to BP-1, where the LLP has a decay length of 10 cm, discrimination is more pronounced for BP-2, where the LLP has a decay length of 100 cm. The plot for $\sum \Delta T$, which shows the sum of the time delay for all the hits in the ECAL, also demonstrates a significant difference between the LLP benchmarks and the background, with a more prominent difference for BP-2. Timing

variable $(\Delta T \times E)_{\text{mean}}^{Max5}$ and $\sum \Delta T$ show comparatively better discrimination between jet timing for QCD and LLP when LLP with lower decay length is considered.

Now, we study the correlation between different timing variables constructed using ECAL timing. Our aim is to identify variables that exhibit high correlation factors for both signal and background while contributing little to distinguish between them. Such redundant variables can be omitted from the analysis, thus improving the efficiency and interpretability of the analysis. Figure 16 and 17 in appendix A illustrates the correlation matrix for the LLP benchmark BP-2 and the QCD background with $H_T^{gen} = \{500 - 600\}$ GeV respectively. As we can see from the figure, several variables show strong correlations with each other for both signal and background. Such variables can be termed redundant and thus excluded from the final analysis. On the other hand, there are some variables showing a strong correlation for a signal while exhibiting a weak correlation for background; such variables can be helpful in distinguishing the signal from the background.

For MVA-2, we follow the same training strategy as outlined in the previous section for MVA-1. However, we utilize a different set of variables to train the XGBoost models as described in this section and listed in the fourth column of table 4. In this case, physics variables are constructed using timing information from the ECAL instead of MTD, as was done for MVA-1. Similar to MVA-1, the main objective of MVA-2 is to identify LLPs with longer lifetimes effectively.

For MVA-2, we have approximately 2200k jets from $t\bar{t}$ events and 1400k jets from QCD dijet events, which are the two dominant background sources. As for the signal benchmark points with decay lengths of 1 cm, 50 cm, and 200 cm, we have approximately 5600k, 5200k, and 4400k jets, respectively.

We now study the performance of three crucial physics variables included in MVA-2 regarding their relative importance in classifying jets in signal and background for three LLP scenarios with decay lengths of 1 cm, 50 cm and 200 cm. Similar to MVA-1, we utilize the gain metric to quantify the importance. The relative feature importance of these variables is shown in figure 12 (left).

As we can see from figure 12 (left), An higher relative importance is assigned to the timing variables, $\Delta T_{\text{mean}}^{ETwt}$ and $(\Delta T \times E)_{\text{mean}}^{Max5}$, for LLPs with larger decay lengths compared to LLPs with smaller decay lengths, as expected. Similarly, p_T^{Ratio} holds more significance for LLPs with larger decay lengths than LLPs with smaller decay lengths. This discrepancy can be understood from the fact that a more significant mismatch arises between the jet p_T calculated using tracks within the jet and the calorimeter jet p_T as the LLP decay length increases, resulting from the fewer displaced tracks being reconstructed.

Here, we would also like to highlight the importance of incorporating energy or transverse energy re-weighting when calculating the timing of the jet. Energy-weighted timing variables exhibit higher significance in classification than timing variables without energy re-weighting. This difference arises from the fact that considering energy-weighted quantities helps mitigate the PU contamination in the jet timing. Since PU energy deposits are soft, their effect on the timing of the jet is reduced after taking their energy into account to construct the jet timing.

In figure 12 (right), we show the ROC curves for three different decay lengths of LLP considering QCD and $t\bar{t}$ background separately, considering the same LLP benchmark scenario

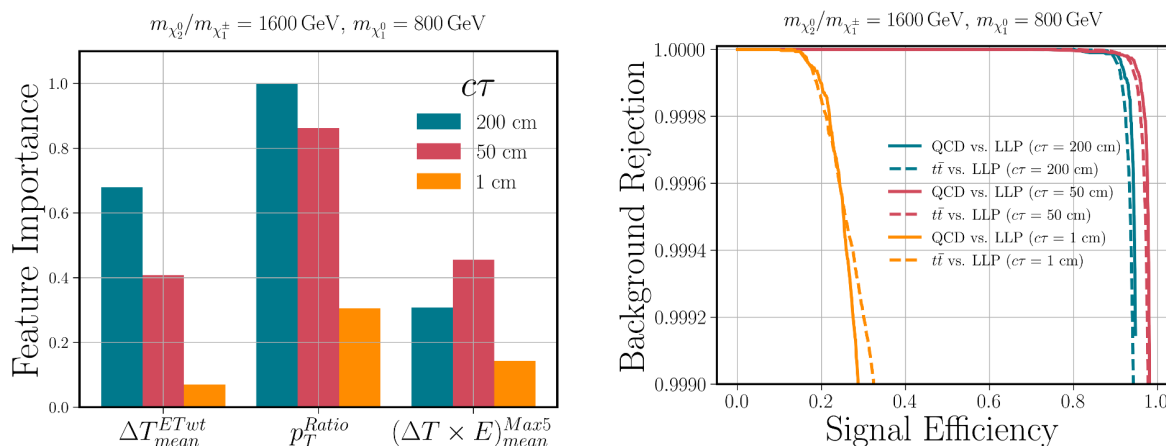


Figure 12. Relative feature importance of three important variables of MVA-2 for three LLP scenarios where decay length is 1 cm, 50 cm and 200 cm (*left*) and classification in terms ROC for two dominant background (QCD and $t\bar{t}$) for LLP with decay length 1 cm, 50 cm and 200 cm (*right*).

Analysis	CBA	MVA-1	MVA-2
Variables	$H_T, N_{\text{trk}}^{\text{disp}}, M_{DV}$	$N_{MTD}, N_{MTD}^{\text{disp}}, N_{MTD}^{NT},$ $T_{\text{raw}}, T_{\text{raw}}^{\text{disp}}, T_{\text{raw}}^{NT},$ $T_{\text{calib}}, T_{\text{calib}}^{\text{disp}}, T_{\text{calib}}^{NT},$ $p_T^{\text{Ratio}}, p_T^{\text{jet}}, \eta^{\text{jet}}$	$\Delta T_{\text{mean}}, \Delta T_{\text{mean}}^{PV}, \Delta T_{\text{mean}}^{PVJ}, \sum \Delta T,$ $\sum \Delta T^{PV}, \sum \Delta T^{PVJ}, \Delta T_{\text{mean}}^{\text{ewt}}, \Delta T_{\text{mean}}^{\text{ewt},PV},$ $\Delta T_{\text{mean}}^{\text{ewt},PVJ}, \Delta T_{\text{mean}}^{\text{etwt}}, \Delta T_{\text{mean}}^{\text{etwt},PV}, \Delta T_{\text{mean}}^{\text{etwt},PVJ},$ $\Delta T_{\text{median}}, \Delta T_{\text{median}}^{PV}, \Delta T_{\text{median}}^{PVJ}, \Delta T_{\text{RMS}},$ $\Delta T_{\text{RMS}}^{PV}, \Delta T_{\text{RMS}}^{PVJ}, \Delta T_{\text{mean}}^{\text{Max5}}, (\Delta T \times E)_{\text{mean}}^{\text{Max5}},$ $(\Delta T \times E)_{\text{mean}}^{\text{TMax5}}, (\Delta T \times E)_{\text{mean}}^{\text{EMax5}},$ $\Delta T_{\text{mean}}^{\text{Max10}}, (\Delta T \times E)_{\text{mean}}^{\text{Max10}},$ $p_T^{\text{Ratio}}, \frac{E_{\text{had}}}{E_{\text{jet}}}, \sum E_{\text{tow}}, N_{\text{trk,prompt}}^{\text{jet}},$ $N_{\text{trk,disp}}^{\text{jet}}, p_T^{\text{jet}}, \eta^{\text{jet}}$

Table 4. Different physics variables to be used in cut-based analysis (CBA) and two independent multi-variate analyses (MVA-1 and MVA-2).

described in the previous section. We can observe that MVA-2 outperforms the LLPs with decay lengths of $c\tau = 50$ cm and 200 cm, compared to 1 cm, emphasizing the vital role of ECAL timing in distinguishing highly displaced LLPs from the background.

In order to make a final selection of events, we impose a criterion that requires at least one jet in each event to have a very high signal probability. This effectively eliminates the majority of the jets originating from background sources.

Next, we will quantify the results obtained from CBA, MVA-1 and MVA-2 in terms of signal significance.

5 Results

The final signal significance is determined by combining the outcomes of MVA-1, MVA-2, and CBA while ensuring that duplicate events are excluded from the final event selection.

Events		Total (mil)	CBA	MVA-1	MVA-2	Combined	Yield	S_{sig}
LLP $M_{\chi_1^0} = 800 \text{ GeV}$ $M_{\chi_2^0} = 1600 \text{ GeV}$	1cm	0.5	444681	29154	49406	447699	215	9.3
	50 cm	0.5	404420	330181	365242	455612	219	9.5
	200 cm	0.5	219169	274411	333449	415166	200	8.6
QCD		3	0	0	0	0	0	—
$t\bar{t}$		5	0	0	1	1	534.0	—
W+Jets		1	0	0	0	0	0	—

Table 5. Total number of events for signal and background obtained individually from the CBA, MVA-1, and MVA-2 analyses, as well as the combined number of events and yield for both signal and background. S_{sig} represents the signal significance for three chosen benchmark points with decay lengths of 1 cm, 50 cm, and 100 cm, and $M_{\chi_2^0} = 1600 \text{ GeV}$ and $M_{\chi_1^0} = 800 \text{ GeV}$.

The signal (S) or background (B) yield is calculated using the following equation,

$$S \text{ or } B = \sigma_{\text{process}} \times \epsilon \times \mathcal{L} \tag{5.1}$$

where σ_{process} represents the production cross-section of the process, ϵ represents the selection efficiency, and \mathcal{L} represents the integrated luminosity. The selection efficiency is determined by dividing the number of finally selected events, obtained after combining the results from MVA-1, MVA-2, and CBA, by the total number of events. In this analysis, integrated luminosity of 3000 fb^{-1} for HL-LHC is considered.

Finally, for each signal benchmark point, we calculate signal significance using the following formula,

$$S_{\text{sig}} = \frac{S}{\sqrt{B}} \tag{5.2}$$

where S_{sig} represents the signal significance, and S and B represent the signal and background yields, respectively.

In table 5, we present the number of events, yield, and signal significance obtained from CBA, MVA-1 and MVA-2 for three LLP benchmark points with decay lengths of 1 cm, 50 cm, 200 cm, and $M_{\chi_2^0} = 1600 \text{ GeV}$ and $M_{\chi_1^0} = 800 \text{ GeV}$, along with three background sources.

We generate 0.5 million events for each LLP benchmark. At L1, where we select events with lepton triggers, displaced calo-jet trigger and track- H_T trigger, LLP events are selected with more than 90% efficiency, with efficiency decreasing as decay length increases. Further, we select events with $H_T > 500 \text{ GeV}$. Since QCD events are generated $H_T^{\text{Gen}} > 500 \text{ GeV}$, most QCD events pass this cut. For CBA, events with at least one secondary vertex with at least six displaced tracks with $M_{DV} > 20 \text{ GeV}$ are selected. Events with LLPs having smaller decay lengths are mostly selected, while signal efficiency decreases with increasing decay length, with efficiency decreasing to less than 50% for decay length above 200 cm. We find no background events passing the criteria mentioned above. The instrumental background is also handled since we require $M_{DV} > 20 \text{ GeV}$. Next, we select jets out of jets selected at L1 after applying suitable cut on signal probability of jets from MVA-1 and MVA-2 separately

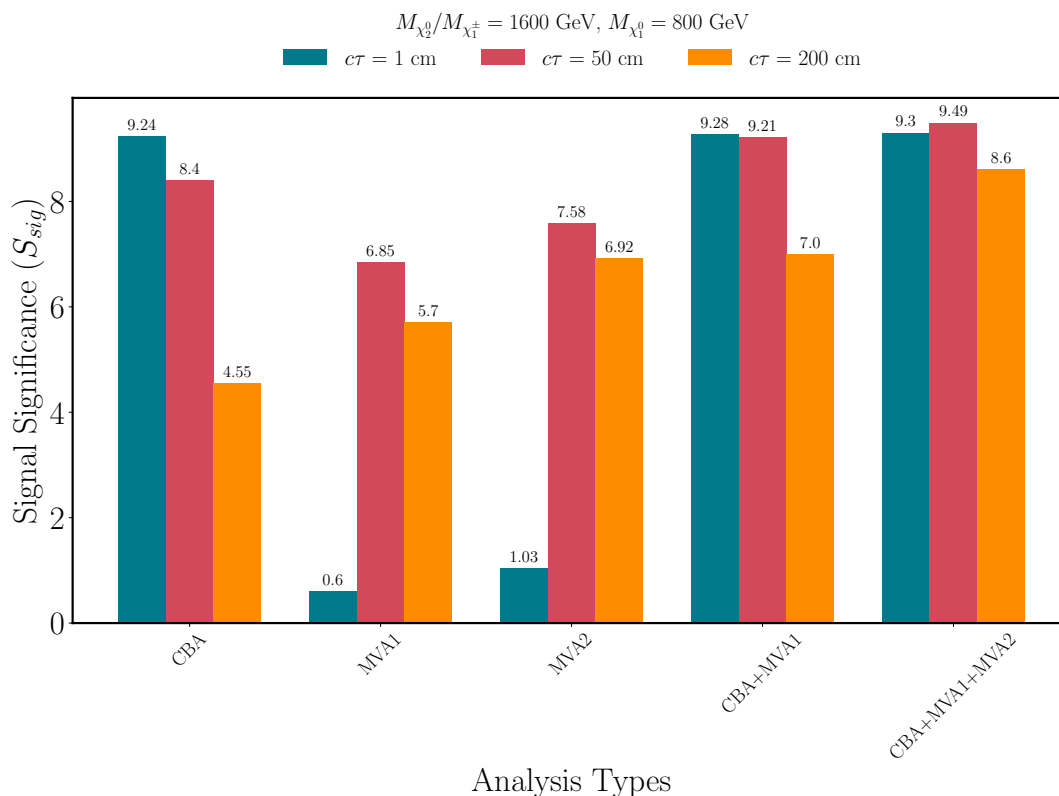


Figure 13. Comparison of signal significance by different analysis strategy types for various benchmark points as tabulated in table 5.

where XGBOOST trained model is applied on L1 jets. Those events are selected where we find at least one jet passing the selection criteria on signal probability.

MVA-1 and MVA-2 surpass CBA in identifying LLPs with 200 cm decay length. Remarkably, MVA-2 outperforms CBA notably for $c\tau = 200 \text{ cm}$. The combined usage of MVA-1 and MVA-2 demonstrates significantly better signal efficiency than CBA alone, emphasizing the importance of timing information when searching for LLPs with long lifetimes. However, as anticipated, MVA-1 and MVA-2 exhibit poor performance for the LLP benchmark with $c\tau = 1 \text{ cm}$ compared to CBA. In table 5, We also show the yield and signal significance for the three benchmark points for the wino-like chargino-neutralino pair production at HL-LHC, considering an integrated luminosity of $\mathcal{L} = 3000 \text{ fb}^{-1}$. We obtain the signal significance of around 9σ for all three decay lengths. Remarkably, signal significance does not degrade with decay length, which is attributed to increased analysis sensitivity to the LLPs with higher decay length, thanks to the inclusion of the timing information in the analysis.

In figure 13, we show the signal significance for three benchmark points as tabulated in table 5 for different analysis strategies – CBA, MVA-1, and MVA-2, as well as their combinations (CBA+MVA1 and CBA+MVA1+MVA2) to signify the importance of MVA-2 in current study.

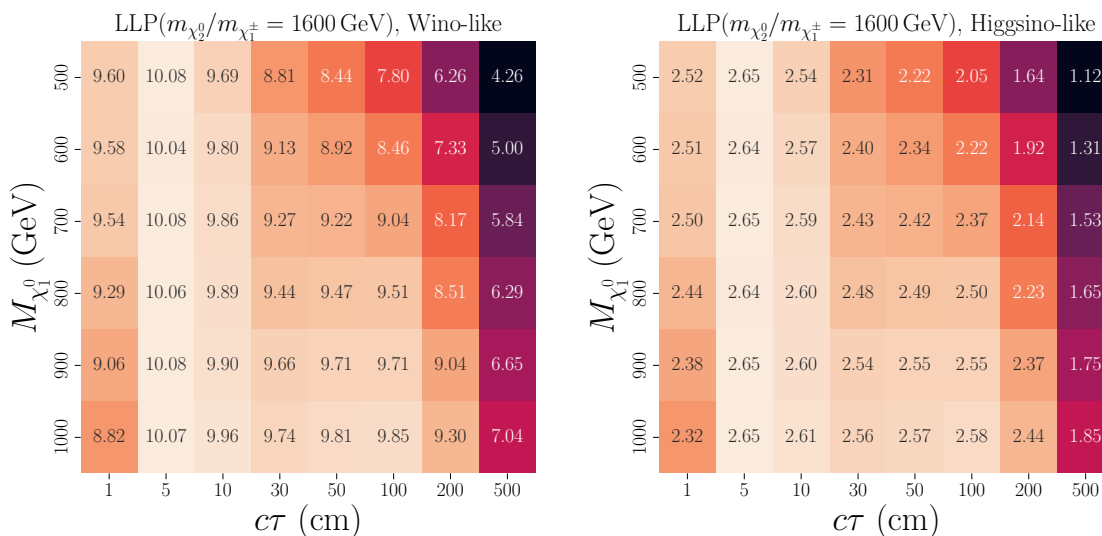


Figure 14. Signal significance for LLP benchmark points with $M_{\chi_2^0} = 1600$ GeV and $M_{\chi_1^0}$ varying from 500 GeV to 1000 GeV while decay length varies from 1 cm to 500 cm for wino and higgsino-like chargino-neutralino pair production.

Figure 13 shows that while the increase in signal significance for LLP benchmark point with a decay length of 1 cm and 50 cm is not substantial when including MVA-2, there is a notable improvement for LLP benchmark with a decay length 200 cm. This finding is particularly relevant given the small signal cross-section in our study, highlighting the importance of MVA-2 in enhancing the sensitivity to LLPs with longer decay lengths.

We extend the analysis by calculating signal significance for a set of LLP benchmark points following the similar procedure as described above and in section 4.1, 4.2, and 4.3. In figure 14, we present the signal significance for numerous LLP benchmark points for wino and higgsino-like $M_{\chi_2^0}/M_{\chi_1^0}$ pair production scenario where $M_{\chi_2^0} = 1600$ GeV and $M_{\chi_1^0}$ varies from 500 GeV to 1000 GeV with decay length varying from 1 cm to 500 cm in the form of a grid. As mentioned earlier, We train three different XGBOOST models for three different decay lengths, namely 1 cm, 50 cm and 200 cm, with $M_{\chi_2^0} = 1600$ and $M_{\chi_1^0} = 800$. The model trained with LLP benchmark with a decay length of 1 cm is applied on LLPs with decay lengths varying between 1 cm and 5 cm. The LLP model trained with a decay length of 50 cm is applied on LLPs with decay lengths between 10 cm and 100 cm, while the LLP model trained with a decay length of 200 cm is reserved for LLPs with very high decay lengths greater than 200 cm.

From figure 14, we observe a general trend: the signal significance tends to decrease as the decay length of LLP increases. This results from fewer LLPs decay within the tracker and calorimeter volumes as the decay length of the LLP increases. Moreover, the signal significance decreases with a decrease in the LLP mass.

For wino-like chargino-neutralino pair production, a maximum signal significance of approximately 10 is observed for LLPs with a decay length of 5 cm across all mass points. At the smallest decay length of 1 cm, the signal significance ranges from 8.82 (for $M_{\chi_1^0} = 1000$ GeV)

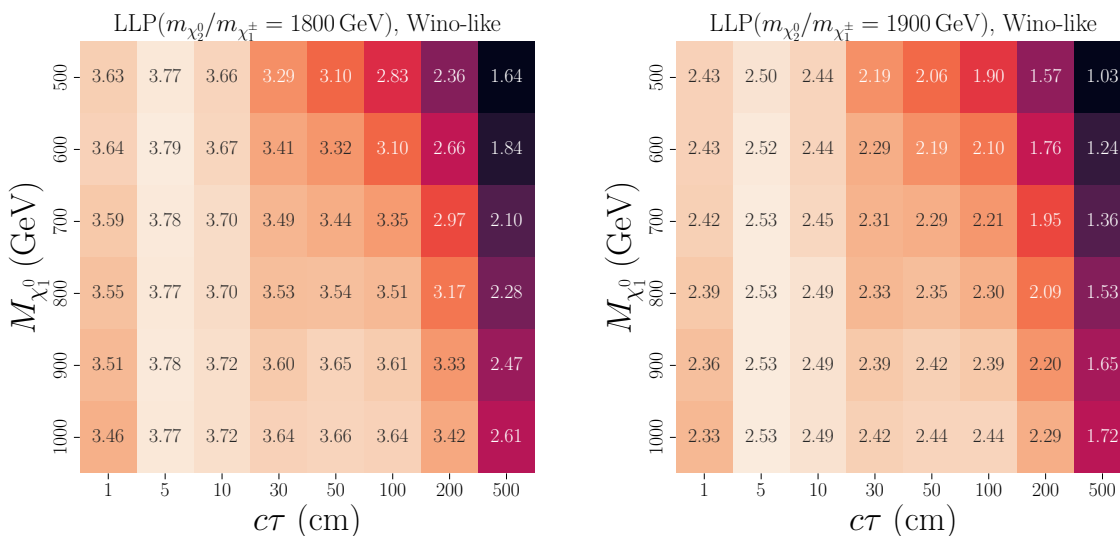


Figure 15. Signal significance for LLP benchmark points with $M_{\chi_2^0} = 1800$ GeV and 1900 GeV and $M_{\chi_1^0}$ varying from 500 GeV to 1000 GeV while decay length varies from 1 cm to 500 cm for wino-like chargino-neutralino pair production.

to 9.60 (for $M_{\chi_1^0} = 500$ GeV). As the decay length increases to the maximum of 500 cm, the signal significance decreases to a range of 7.04 (for $M_{\chi_1^0} = 1000$ GeV) and 4.26 (for $M_{\chi_1^0} = 500$ GeV). For $M_{\chi_1^0} = 800$ GeV, the signal significance starts at 9.29 for LLP with a 1 cm decay length and drops to 6.29 at a 500 cm decay length. This decrease in signal significance with increasing decay length is consistent across all mass points. Regarding probing and discovery potential at HL-LHC, all mass points exhibit a signal significance greater than two across all decay lengths, implying the potential for probing at the HL-LHC. For discovery potential at the HL-LHC, defined as a signal significance greater than 5 , our analysis suggests that all mass points maintain discovery potential up to a decay length of 500 cm except for $M_{\chi_1^0} = 500$ GeV at 500 cm decay length.

For higgsino-like chargino-neutralino pair production with a relatively smaller cross-section than a wino-like signature, a maximum signal significance of approximately 2.6 is observed for LLP benchmark points with decay lengths greater than 5 cm and 10 cm across all LLP mass points. At a decay length of 1 cm, the signal significance varies from 2.52 (at $M_{\chi_1^0} = 500$ GeV) to 2.32 (at $M_{\chi_1^0} = 1000$ GeV). As the decay length extends to 500 cm, the signal significance decreases, with values ranging from 1.85 (at $M_{\chi_1^0} = 1000$ GeV) to 1.12 (at $M_{\chi_1^0} = 500$ GeV). When considering the probing potential at the HL-LHC, it is important to note that all mass points maintain a signal significance greater than 2 for decay lengths up to 200 cm, except for the LLPs with 500 and 600 GeV mass at a decay length of 200 cm. It is worth mentioning that signal significance increases with the mass of the LLPs. Thus, LLPs with a mass greater than 1000 GeV and a decay length of 500 cm have the potential to be probed at HL-LHC.

We also present signal significance for wino-like chargino-neutralino pair production for $M_{\chi_2^0} = 1800$ GeV and 1900 GeV as shown in figure 15.

For $M_{\chi_2^0} = 1800$ GeV, we observe a maximum signal significance of ≈ 3.8 at $M_{\chi_1^0} = 600$ GeV with a 5 cm decay length. LLPs with mass $M_{\chi_1^0} > 600$ GeV maintain a signal significance over two at a decay length of 500 cm, indicating the potential for probing at the HL-LHC. For $M_{\chi_2^0} = 1900$ GeV, signal significance generally decreases with increased decay lengths, but higher mass points retain better values, suggesting a stronger HL-LHC probing potential. Particularly at the decay length of 200 cm, all mass points from $M_{\chi_1^0} = 800$ GeV and above maintain signal significance above the threshold of 2. For LLP with $M_{\chi_1^0} = 1000$ GeV and 500 cm decay length, a signal significance of 1.72 is observed, which is close to the probing threshold. Furthermore, as the mass of the LLPs at the decay length of 500 cm increases, the signal significance is expected to rise further. Therefore, LLPs with masses greater than 1000 GeV could be probed at HL-LHC.

6 Summary and conclusion

The exploration of supersymmetry (SUSY) continues to be crucial in investigating physics beyond the Standard Model, driven by strong theoretical and phenomenological motivations. Although both R-parity conserving and violating scenarios of SUSY have been extensively studied using prompt physics signatures, there is a scarcity of realistic phenomenological studies targeting the search for SUSY via exotic displaced signatures in R-parity violating (RPV) SUSY, especially in the context of HL-LHC. In this work, we particularly analyze the pair production of electroweakinos, χ_2^0 and χ_1^\pm , and their decay into Higgs boson and W boson, respectively, along with χ_1^0 . The χ_1^0 then undergo further decay to light quarks, facilitated by small values of the RPV couplings λ'' , resulting in χ_1^0 with longer lifetimes.

In order to select events at the Level-1 trigger level efficiently, we have used three triggers: track- H_T , Displaced Calo-Jet, and Single TkIsoLepton. The first two triggers are specifically designed for displaced searches. Our analysis shows that the Displaced Calo-Jet trigger is highly effective in selecting long-lived particle (LLP) events where LLP has a longer lifetime, while the Track- H_T trigger is primarily efficient in selecting LLP events with smaller decay lengths. By combining these three triggers, we demonstrate the ability to effectively select LLP events across a wide range of decay lengths, ranging from very small to very high, with a high level of efficiency. This highlights the complementary nature of these triggers in capturing LLP signatures with varying decay lengths and underscores their effectiveness in our study. In the following step, we construct several physics variables by utilizing information from the tracker, MTD, and calorimeters. The analysis is subdivided into three parts, namely cut-based analysis (CBA), multivariate analysis-1 (MVA-1), and multivariate analysis-2 (MVA-2). The cut-based analysis incorporates displaced vertex information, while MVA-1 and MVA-2 employ timing information from MTD and ECAL, respectively. Our findings indicate that LLPs with shorter decay lengths can be effectively searched using the cut-based analysis. However, for LLPs with longer decay lengths, where displaced vertex information alone may not be sufficient, timing-based analyses such as MVA-1 and MVA-2 provide effective selection methods. These results contribute to the understanding of the best approaches for identifying LLPs in different decay length scenarios, considering the limitations of displaced vertex information and the potential of timing-based analyses in the context of this study.

Finally, we calculate the signal significance for LLPs in different benchmark scenarios. We vary the mass of LLPs from 500 GeV to 1000 GeV and the decay length from 1 cm to 500 cm for both wino-like and higgsino-like electroweakino pair production scenarios, with a degenerate chargino/neutralino mass, $M_{\chi_2^0}/M_{\chi_1^\pm} = 1600$ GeV. Our results show that LLPs in the wino-like chargino/neutralino pair production scenario, for all benchmark points discussed, have the potential to be probed at the HL-LHC with signal significance greater than or equal to 5σ for all LLP masses except for LLP with mass 500 GeV at 500 cm decay length where signal significance is less than 5 but greater than 2. However, the significance decreases for the higgsino-like scenario. Nonetheless, the majority of the benchmark points exhibit signal significance greater than 2σ except for LLPs at 500 cm decay length and LLPs with mass ≤ 600 GeV at 200 cm decay length, suggesting that they can be probed at the HL-LHC. In comparison, the ATLAS study [58] which examines the pair production of electroweakinos in four channels in a pure higgsino state, using the processes $pp \rightarrow \chi_1^\pm \chi_2^0, \chi_2^0 \chi_1^0, \chi_1^+ \chi_1^-,$ and $\chi_1^\pm \chi_1^0$ at 13 TeV, rules out electroweakinos with masses below roughly 1250 GeV for a decay length of 200 cm. Our analysis, focusing only on the $\chi_1^\pm \chi_2^0$ production channel, projects the exclusion mass limit for electroweakinos to 1600 GeV at the same decay length.

We also calculate the signal significance for the heavier electroweakinos with $M_{\chi_2^0}/M_{\chi_1^\pm}$ of 1800 and 1900 GeV for wino-like LLP signatures. For $M_{\chi_2^0}/M_{\chi_1^\pm} = 1800$ GeV, all mass points, except for $M_{\chi_1^0} \leq 600$ GeV, retain a signal significance above 2 across all decay lengths. For $M_{\chi_2^0} = 1900$ GeV, Despite the general decrease in signal significance with increased decay lengths, higher mass points sustain stronger values, thereby indicating their probing potential at HL-LHC. Particularly, all mass points from $M_{\chi_1^0} = 800$ GeV and higher maintain a signal significance above 2 at a decay length of 200 cm, indicating their probing potential at HL-LHC.

Acknowledgments

BB acknowledges the support provided by the MATRICS Grant(MTR/2022/000264) of the Science and Engineering Research Board (SERB), Government of India. PS thanks Rhitaja Sengupta for the valuable discussions. This work utilized the computing facility at the Centre for High Energy Physics (CHEP), IISc.

A Correlation matrix for ECAL timing variables

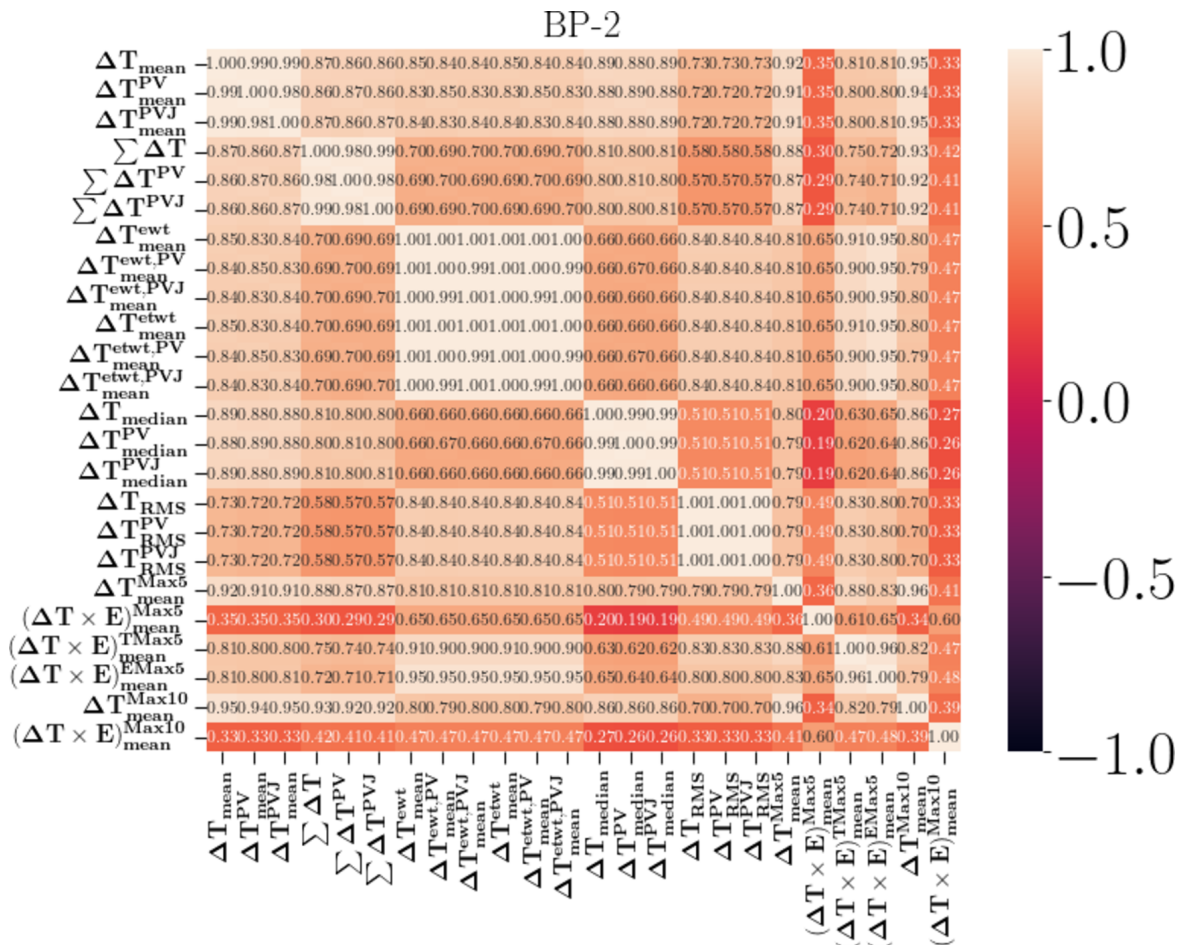


Figure 16. Correlation between different timing variables constructed using information from ECAL for signal (BP-2).

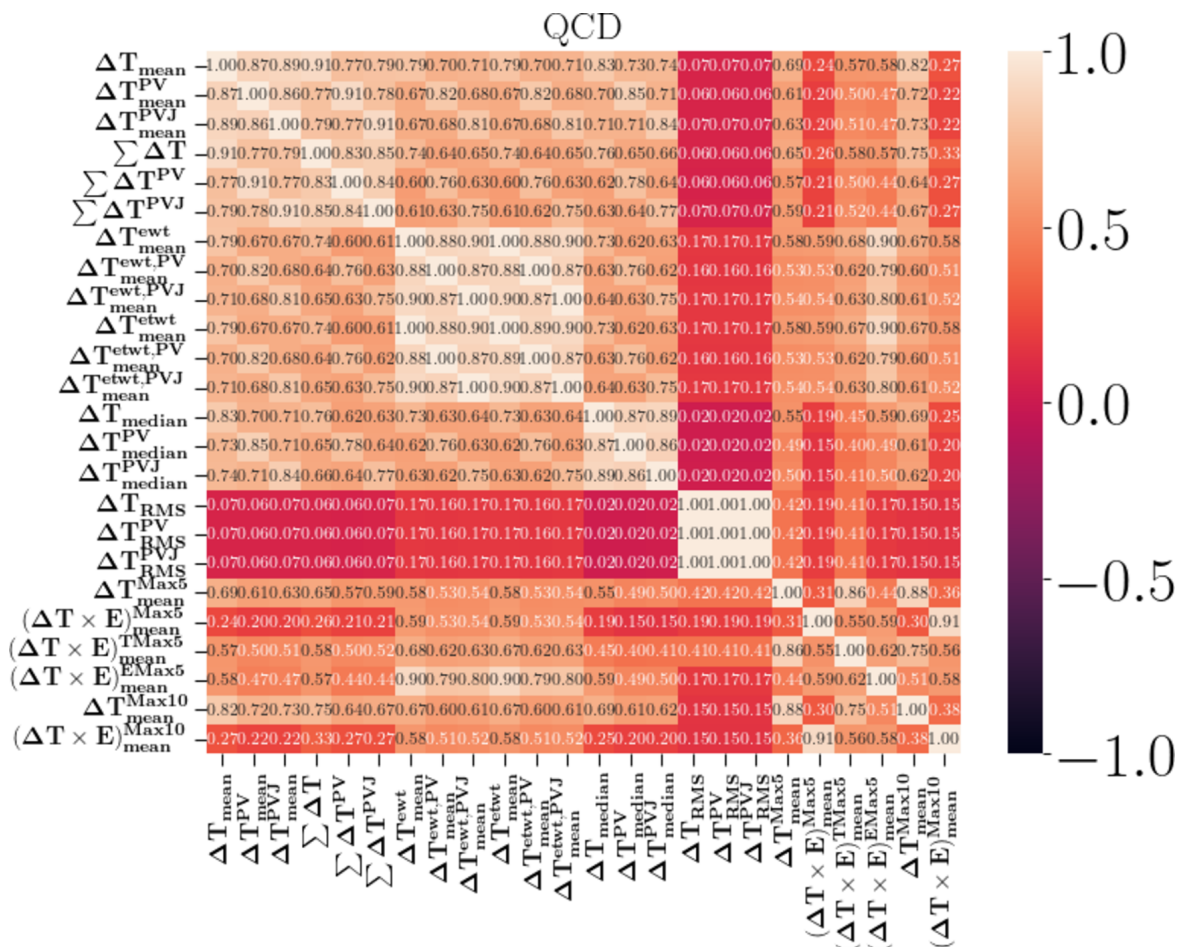


Figure 17. Correlation between different timing variables constructed using information from ECAL for background (QCD).

Open Access. This article is distributed under the terms of the Creative Commons Attribution License ([CC-BY4.0](https://creativecommons.org/licenses/by/4.0/)), which permits any use, distribution and reproduction in any medium, provided the original author(s) and source are credited.

References

- [1] P. Ilten, J. Thaler, M. Williams and W. Xue, *Dark photons from charm mesons at LHCb*, *Phys. Rev. D* **92** (2015) 115017 [[arXiv:1509.06765](https://arxiv.org/abs/1509.06765)] [[INSPIRE](https://inspirehep.net/literature/1371100)].
- [2] A.M. Gago et al., *Probing the type I seesaw mechanism with displaced vertices at the LHC*, *Eur. Phys. J. C* **75** (2015) 470 [[arXiv:1505.05880](https://arxiv.org/abs/1505.05880)] [[INSPIRE](https://inspirehep.net/literature/1328100)].
- [3] S. Banerjee et al., *Novel signature for long-lived particles at the LHC*, *Phys. Rev. D* **98** (2018) 115026 [[arXiv:1706.07407](https://arxiv.org/abs/1706.07407)] [[INSPIRE](https://inspirehep.net/literature/1644000)].
- [4] R. Kumar Barman et al., *Scope of self-interacting thermal WIMPs in a minimal $U(1)_D$ extension and its future prospects*, *JHEP* **05** (2019) 177 [[arXiv:1811.09195](https://arxiv.org/abs/1811.09195)] [[INSPIRE](https://inspirehep.net/literature/1811091)].
- [5] B. Bhattacharjee, S. Mukherjee and R. Sengupta, *Study of energy deposition patterns in hadron calorimeter for prompt and displaced jets using convolutional neural network*, *JHEP* **11** (2019) 156 [[arXiv:1904.04811](https://arxiv.org/abs/1904.04811)] [[INSPIRE](https://inspirehep.net/literature/1904048)].

- [6] X. Cid Vidal, Y. Tsai and J. Zurita, *Exclusive displaced hadronic signatures in the LHC forward region*, *JHEP* **01** (2020) 115 [[arXiv:1910.05225](#)] [[INSPIRE](#)].
- [7] S. Banerjee et al., *Determining the lifetime of long-lived particles at the HL-LHC*, *Eur. Phys. J. C* **81** (2021) 172 [[arXiv:1912.06669](#)] [[INSPIRE](#)].
- [8] J. Jones-Pérez, J. Masias and J.D. Ruiz-Álvarez, *Search for long-lived heavy neutrinos at the LHC with a VBF trigger*, *Eur. Phys. J. C* **80** (2020) 642 [[arXiv:1912.08206](#)] [[INSPIRE](#)].
- [9] B. Bhattacharjee, S. Mukherjee, R. Sengupta and P. Solanki, *Triggering long-lived particles in HL-LHC and the challenges in the rst stage of the trigger system*, *JHEP* **08** (2020) 141 [[arXiv:2003.03943](#)] [[INSPIRE](#)].
- [10] B. Bhattacharjee, T. Ghosh, R. Sengupta and P. Solanki, *Dedicated triggers for displaced jets using timing information from electromagnetic calorimeter at HL-LHC*, *JHEP* **08** (2022) 254 [[arXiv:2112.04518](#)] [[INSPIRE](#)].
- [11] A. Adhikary et al., *Long-lived NLSP in the NMSSM*, *Phys. Rev. D* **108** (2023) 035020 [[arXiv:2207.00600](#)] [[INSPIRE](#)].
- [12] Y. Gershtein, S. Knapen and D. Redigolo, *Probing naturally light singlets with a displaced vertex trigger*, *Phys. Lett. B* **823** (2021) 136758 [[arXiv:2012.07864](#)] [[INSPIRE](#)].
- [13] E. Fuchs, O. Matsedonskyi, I. Savoray and M. Schlaffer, *Collider searches for scalar singlets across lifetimes*, *JHEP* **04** (2021) 019 [[arXiv:2008.12773](#)] [[INSPIRE](#)].
- [14] K. Cheung, O. Fischer, Z.S. Wang and J. Zurita, *Exotic Higgs decays into displaced jets at the LHeC*, *JHEP* **02** (2021) 161 [[arXiv:2008.09614](#)] [[INSPIRE](#)].
- [15] J. Liu, Z. Liu, L.-T. Wang and X.-P. Wang, *Enhancing sensitivities to long-lived particles with high granularity calorimeters at the LHC*, *JHEP* **11** (2020) 066 [[arXiv:2005.10836](#)] [[INSPIRE](#)].
- [16] J.A. Evans, A. Gandrakota, S. Knapen and H. Routray, *Searching for exotic B-meson decays enabled by the CMS L1 track trigger*, *Phys. Rev. D* **103** (2021) 015026 [[arXiv:2008.06918](#)] [[INSPIRE](#)].
- [17] D. Linthorne and D. Stolarski, *Triggering on emerging jets*, *Phys. Rev. D* **104** (2021) 035019 [[arXiv:2103.08620](#)] [[INSPIRE](#)].
- [18] D. Acosta et al., *Review of opportunities for new long-lived particle triggers in run 3 of the Large Hadron Collider*, [arXiv:2110.14675](#) [[INSPIRE](#)].
- [19] B. Bhattacharjee, S. Matsumoto and R. Sengupta, *Long-lived light mediators from Higgs boson decay at HL-LHC and FCC-hh, and a proposal of dedicated long-lived particle detectors for FCC-hh*, *Phys. Rev. D* **106** (2022) 095018 [[arXiv:2111.02437](#)] [[INSPIRE](#)].
- [20] K. Sakurai and W. Yin, *Phenomenology of CP-even ALP*, *JHEP* **04** (2022) 113 [[arXiv:2111.03653](#)] [[INSPIRE](#)].
- [21] M. Du, R. Fang, Z. Liu and V.Q. Tran, *Enhanced long-lived dark photon signals at lifetime frontier detectors*, *Phys. Rev. D* **105** (2022) 055012 [[arXiv:2111.15503](#)] [[INSPIRE](#)].
- [22] B. Bhattacharjee, P. Konar, V.S. Ngairangbam and P. Solanki, *LLPNet: graph autoencoder for triggering light long-lived particles at HL-LHC*, [arXiv:2308.13611](#) [[INSPIRE](#)].
- [23] CMS collaboration, *Search for long-lived particles that decay into final states containing two electrons or two muons in proton-proton collisions at $\sqrt{s} = 8$ TeV*, *Phys. Rev. D* **91** (2015) 052012 [[arXiv:1411.6977](#)] [[INSPIRE](#)].
- [24] CMS collaboration, *Search for displaced leptons in the $e\text{-}\mu$ channel*, CMS-PAS-EXO-16-022, CERN, Geneva, Switzerland (2016).

- [25] CMS collaboration, *Search for heavy stable charged particles with 12.9 fb^{-1} of 2016 data*, [CMS-PAS-EXO-16-036](#), CERN, Geneva, Switzerland (2016).
- [26] CMS collaboration, *Search for decays of stopped exotic long-lived particles produced in proton-proton collisions at $\sqrt{s} = 13 \text{ TeV}$* , *JHEP* **05** (2018) 127 [[arXiv:1801.00359](#)] [[INSPIRE](#)].
- [27] CMS collaboration, *Search for pair production of second-generation leptoquarks at $\sqrt{s} = 13 \text{ TeV}$* , *Phys. Rev. D* **99** (2019) 032014 [[arXiv:1808.05082](#)] [[INSPIRE](#)].
- [28] CMS collaboration, *Search for new particles decaying to a jet and an emerging jet*, *JHEP* **02** (2019) 179 [[arXiv:1810.10069](#)] [[INSPIRE](#)].
- [29] CMS collaboration, *Search sensitivity for dark photons decaying to displaced muons with CMS at the high-luminosity LHC*, [CMS-PAS-FTR-18-002](#), CERN, Geneva, Switzerland (2018).
- [30] CMS collaboration, *Search for long-lived particles decaying to jets with displaced vertices*, [CMS-PAS-EXO-19-013](#), CERN, Geneva, Switzerland (2020).
- [31] CMS collaboration, *Search for long-lived particles using nonprompt jets and missing transverse momentum with proton-proton collisions at $\sqrt{s} = 13 \text{ TeV}$* , *Phys. Lett. B* **797** (2019) 134876 [[arXiv:1906.06441](#)] [[INSPIRE](#)].
- [32] CMS collaboration, *Search for long-lived particles using delayed photons in proton-proton collisions at $\sqrt{s} = 13 \text{ TeV}$* , *Phys. Rev. D* **100** (2019) 112003 [[arXiv:1909.06166](#)] [[INSPIRE](#)].
- [33] CMS collaboration, *Search for disappearing tracks in proton-proton collisions at $\sqrt{s} = 13 \text{ TeV}$* , *Phys. Lett. B* **806** (2020) 135502 [[arXiv:2004.05153](#)] [[INSPIRE](#)].
- [34] CMS collaboration, *Search for long-lived particles using displaced jets in proton-proton collisions at $\sqrt{s} = 13 \text{ TeV}$* , *Phys. Rev. D* **104** (2021) 012015 [[arXiv:2012.01581](#)] [[INSPIRE](#)].
- [35] CMS collaboration, *Search for long-lived particles decaying in the CMS end cap muon detectors in proton-proton collisions at $\sqrt{s} = 13 \text{ TeV}$* , *Phys. Rev. Lett.* **127** (2021) 261804 [[arXiv:2107.04838](#)] [[INSPIRE](#)].
- [36] CMS collaboration, *Search for long-lived particles decaying to leptons with large impact parameter in proton-proton collisions at $\sqrt{s} = 13 \text{ TeV}$* , *Eur. Phys. J. C* **82** (2022) 153 [[arXiv:2110.04809](#)] [[INSPIRE](#)].
- [37] CMS collaboration, *Search for long-lived particles produced in association with a Z boson in proton-proton collisions at $\sqrt{s} = 13 \text{ TeV}$* , *JHEP* **03** (2022) 160 [[arXiv:2110.13218](#)] [[INSPIRE](#)].
- [38] CMS collaboration, *Search for long-lived particles using out-of-time trackless jets in proton-proton collisions at $\sqrt{s} = 13 \text{ TeV}$* , *JHEP* **07** (2023) 210 [[arXiv:2212.06695](#)] [[INSPIRE](#)].
- [39] ATLAS collaboration, *Search for long-lived, weakly interacting particles that decay to displaced hadronic jets in proton-proton collisions at $\sqrt{s} = 8 \text{ TeV}$ with the ATLAS detector*, *Phys. Rev. D* **92** (2015) 012010 [[arXiv:1504.03634](#)] [[INSPIRE](#)].
- [40] ATLAS collaboration, *Search for metastable heavy charged particles with large ionisation energy loss in pp collisions at $\sqrt{s} = 8 \text{ TeV}$ using the ATLAS experiment*, *Eur. Phys. J. C* **75** (2015) 407 [[arXiv:1506.05332](#)] [[INSPIRE](#)].
- [41] ATLAS collaboration, *A search for prompt lepton-jets in pp collisions at $\sqrt{s} = 8 \text{ TeV}$ with the ATLAS detector*, *JHEP* **02** (2016) 062 [[arXiv:1511.05542](#)] [[INSPIRE](#)].
- [42] ATLAS collaboration, *Search for long-lived, massive particles in events with displaced vertices and missing transverse momentum in $\sqrt{s} = 13 \text{ TeV}$ pp collisions with the ATLAS detector*, *Phys. Rev. D* **97** (2018) 052012 [[arXiv:1710.04901](#)] [[INSPIRE](#)].

- [43] ATLAS collaboration, *Search for long-lived particles in final states with displaced dimuon vertices in pp collisions at $\sqrt{s} = 13$ TeV with the ATLAS detector*, *Phys. Rev. D* **99** (2019) 012001 [[arXiv:1808.03057](#)] [[INSPIRE](#)].
- [44] ATLAS collaboration, *Search for heavy charged long-lived particles in proton-proton collisions at $\sqrt{s} = 13$ TeV using an ionisation measurement with the ATLAS detector*, *Phys. Lett. B* **788** (2019) 96 [[arXiv:1808.04095](#)] [[INSPIRE](#)].
- [45] ATLAS collaboration, *Search for the production of a long-lived neutral particle decaying within the ATLAS hadronic calorimeter in association with a Z boson from pp collisions at $\sqrt{s} = 13$ TeV*, *Phys. Rev. Lett.* **122** (2019) 151801 [[arXiv:1811.02542](#)] [[INSPIRE](#)].
- [46] ATLAS collaboration, *Search for long-lived particles produced in pp collisions at $\sqrt{s} = 13$ TeV that decay into displaced hadronic jets in the ATLAS muon spectrometer*, *Phys. Rev. D* **99** (2019) 052005 [[arXiv:1811.07370](#)] [[INSPIRE](#)].
- [47] ATLAS collaboration, *Search for long-lived neutral particles in pp collisions at $\sqrt{s} = 13$ TeV that decay into displaced hadronic jets in the ATLAS calorimeter*, *Eur. Phys. J. C* **79** (2019) 481 [[arXiv:1902.03094](#)] [[INSPIRE](#)].
- [48] ATLAS collaboration, *Search for heavy neutral leptons in decays of W bosons produced in 13 TeV pp collisions using prompt and displaced signatures with the ATLAS detector*, *JHEP* **10** (2019) 265 [[arXiv:1905.09787](#)] [[INSPIRE](#)].
- [49] ATLAS collaboration, *Search for displaced vertices of oppositely charged leptons from decays of long-lived particles in pp collisions at $\sqrt{s} = 13$ TeV with the ATLAS detector*, *Phys. Lett. B* **801** (2020) 135114 [[arXiv:1907.10037](#)] [[INSPIRE](#)].
- [50] ATLAS collaboration, *Search for light long-lived neutral particles produced in pp collisions at $\sqrt{s} = 13$ TeV and decaying into collimated leptons or light hadrons with the ATLAS detector*, *Eur. Phys. J. C* **80** (2020) 450 [[arXiv:1909.01246](#)] [[INSPIRE](#)].
- [51] ATLAS collaboration, *Search for long-lived neutral particles produced in pp collisions at $\sqrt{s} = 13$ TeV decaying into displaced hadronic jets in the ATLAS inner detector and muon spectrometer*, *Phys. Rev. D* **101** (2020) 052013 [[arXiv:1911.12575](#)] [[INSPIRE](#)].
- [52] ATLAS collaboration, *Search prospects for dark-photons decaying to displaced collimated jets of muons at HL-LHC*, ATLAS-PHYS-PUB-2019-002, CERN, Geneva, Switzerland (2019).
- [53] ATLAS collaboration, *Search for long-lived, massive particles in events with a displaced vertex and a muon with large impact parameter in pp collisions at $\sqrt{s} = 13$ TeV with the ATLAS detector*, *Phys. Rev. D* **102** (2020) 032006 [[arXiv:2003.11956](#)] [[INSPIRE](#)].
- [54] ATLAS collaboration, *Search for long-lived charginos based on a disappearing-track signature using 136 fb^{-1} of pp collisions at $\sqrt{s} = 13$ TeV with the ATLAS detector*, *Eur. Phys. J. C* **82** (2022) 606 [[arXiv:2201.02472](#)] [[INSPIRE](#)].
- [55] ATLAS collaboration, *Search for events with a pair of displaced vertices from long-lived neutral particles decaying into hadronic jets in the ATLAS muon spectrometer in pp collisions at $\sqrt{s} = 13$ TeV*, *Phys. Rev. D* **106** (2022) 032005 [[arXiv:2203.00587](#)] [[INSPIRE](#)].
- [56] ATLAS collaboration, *Search for displaced leptons in $\sqrt{s} = 13$ TeV pp collisions with the ATLAS detector*, *Phys. Rev. Lett.* **127** (2021) 051802 [[arXiv:2011.07812](#)] [[INSPIRE](#)].
- [57] ATLAS collaboration, *Search for exotic decays of the Higgs boson into long-lived particles in pp collisions at $\sqrt{s} = 13$ TeV using displaced vertices in the ATLAS inner detector*, *JHEP* **11** (2021) 229 [[arXiv:2107.06092](#)] [[INSPIRE](#)].

- [58] ATLAS collaboration, *Search for long-lived, massive particles in events with displaced vertices and multiple jets in pp collisions at $\sqrt{s} = 13$ TeV with the ATLAS detector*, *JHEP* **06** (2023) 200 [[arXiv:2301.13866](#)] [[INSPIRE](#)].
- [59] LHCb collaboration, *Search for Higgs-like bosons decaying into long-lived exotic particles*, *Eur. Phys. J. C* **76** (2016) 664 [[arXiv:1609.03124](#)] [[INSPIRE](#)].
- [60] LHCb collaboration, *Search for massive long-lived particles decaying semileptonically in the LHCb detector*, *Eur. Phys. J. C* **77** (2017) 224 [[arXiv:1612.00945](#)] [[INSPIRE](#)].
- [61] LHCb collaboration, *Search for long-lived scalar particles in $B^+ \rightarrow K^+ \chi(\mu^+ \mu^-)$ decays*, *Phys. Rev. D* **95** (2017) 071101 [[arXiv:1612.07818](#)] [[INSPIRE](#)].
- [62] LHCb collaboration, *Updated search for long-lived particles decaying to jet pairs*, *Eur. Phys. J. C* **77** (2017) 812 [[arXiv:1705.07332](#)] [[INSPIRE](#)].
- [63] LHCb collaboration, *Search for $A' \rightarrow \mu^+ \mu^-$ decays*, *Phys. Rev. Lett.* **124** (2020) 041801 [[arXiv:1910.06926](#)] [[INSPIRE](#)].
- [64] LHCb collaboration, *Search for long-lived particles decaying to $e^\pm \mu^\mp \nu$* , *Eur. Phys. J. C* **81** (2021) 261 [[arXiv:2012.02696](#)] [[INSPIRE](#)].
- [65] LHCb collaboration, *Search for massive long-lived particles decaying semileptonically at $\sqrt{s} = 13$ TeV*, *Eur. Phys. J. C* **82** (2022) 373 [[arXiv:2110.07293](#)] [[INSPIRE](#)].
- [66] J.L. Feng, I. Galon, F. Kling and S. Trojanowski, *ForwArd Search ExpeRiment at the LHC*, *Phys. Rev. D* **97** (2018) 035001 [[arXiv:1708.09389](#)] [[INSPIRE](#)].
- [67] D. Curtin et al., *Long-lived particles at the energy frontier: the MATHUSLA physics case*, *Rept. Prog. Phys.* **82** (2019) 116201 [[arXiv:1806.07396](#)] [[INSPIRE](#)].
- [68] C. Alpigiani, *Exploring the lifetime and cosmic frontier with the MATHUSLA detector*, *2020 JINST* **15** C09048 [[arXiv:2006.00788](#)] [[INSPIRE](#)].
- [69] V.V. Gligorov, S. Knapen, M. Papucci and D.J. Robinson, *Searching for long-lived particles: a compact detector for exotics at LHCb*, *Phys. Rev. D* **97** (2018) 015023 [[arXiv:1708.09395](#)] [[INSPIRE](#)].
- [70] G. Aielli et al., *Expression of interest for the CODEX-b detector*, *Eur. Phys. J. C* **80** (2020) 1177 [[arXiv:1911.00481](#)] [[INSPIRE](#)].
- [71] M. Chrzęszcz, M. Drewes and J. Hajer, *HECATE: a long-lived particle detector concept for the FCC-ee or CEPC*, *Eur. Phys. J. C* **81** (2021) 546 [[arXiv:2011.01005](#)] [[INSPIRE](#)].
- [72] R. Schäfer, F. Tillinger and S. Westhoff, *Near or far detectors? A case study for long-lived particle searches at electron-positron colliders*, *Phys. Rev. D* **107** (2023) 076022 [[arXiv:2202.11714](#)] [[INSPIRE](#)].
- [73] B. Bhattacharjee et al., *Light long-lived particles at the FCC-hh with the proposal for a dedicated forward detector FOREHUNT and a transverse detector DELIGHT*, [arXiv:2306.11803](#) [[INSPIRE](#)].
- [74] J. Wess and B. Zumino, *Supergauge transformations in four-dimensions*, *Nucl. Phys. B* **70** (1974) 39 [[INSPIRE](#)].
- [75] H.P. Nilles, *Supersymmetry, supergravity and particle physics*, *Phys. Rept.* **110** (1984) 1 [[INSPIRE](#)].
- [76] H.E. Haber and G.L. Kane, *The search for supersymmetry: probing physics beyond the Standard Model*, *Phys. Rept.* **117** (1985) 75 [[INSPIRE](#)].

- [77] R. Barbier et al., *R-parity violating supersymmetry*, *Phys. Rept.* **420** (2005) 1 [[hep-ph/0406039](#)] [[INSPIRE](#)].
- [78] D. Hooper and T. Plehn, *Supersymmetric dark matter: how light can the LSP be?*, *Phys. Lett. B* **562** (2003) 18 [[hep-ph/0212226](#)] [[INSPIRE](#)].
- [79] N. Bhattacharyya, A. Choudhury and A. Datta, *Low mass neutralino dark matter in mSUGRA and more general models in the light of LHC data*, *Phys. Rev. D* **84** (2011) 095006 [[arXiv:1107.1997](#)] [[INSPIRE](#)].
- [80] D. Albornoz Vasquez, G. Belanger and C. Boehm, *Revisiting light neutralino scenarios in the MSSM*, *Phys. Rev. D* **84** (2011) 095015 [[arXiv:1108.1338](#)] [[INSPIRE](#)].
- [81] A. Choudhury and A. Datta, *Many faces of low mass neutralino dark matter in the unconstrained MSSM, LHC data and new signals*, *JHEP* **06** (2012) 006 [[arXiv:1203.4106](#)] [[INSPIRE](#)].
- [82] A. Fowlie et al., *Dark matter and collider signatures of the MSSM*, *Phys. Rev. D* **88** (2013) 055012 [[arXiv:1306.1567](#)] [[INSPIRE](#)].
- [83] L. Roszkowski, E.M. Sessolo and A.J. Williams, *Prospects for dark matter searches in the pMSSM*, *JHEP* **02** (2015) 014 [[arXiv:1411.5214](#)] [[INSPIRE](#)].
- [84] K. Hamaguchi and K. Ishikawa, *Prospects for Higgs- and Z-resonant neutralino dark matter*, *Phys. Rev. D* **93** (2016) 055009 [[arXiv:1510.05378](#)] [[INSPIRE](#)].
- [85] T. Han, Z. Liu and S. Su, *Light neutralino dark matter: direct/indirect detection and collider searches*, *JHEP* **08** (2014) 093 [[arXiv:1406.1181](#)] [[INSPIRE](#)].
- [86] G. Bélanger et al., *LHC constraints on light neutralino dark matter in the MSSM*, *Phys. Lett. B* **726** (2013) 773 [[arXiv:1308.3735](#)] [[INSPIRE](#)].
- [87] B. Ananthanarayan, J. Lahiri, P.N. Pandita and M. Patra, *Invisible decays of the lightest Higgs boson in supersymmetric models*, *Phys. Rev. D* **87** (2013) 115021 [[arXiv:1306.1291](#)] [[INSPIRE](#)].
- [88] H.K. Dreiner, J.S. Kim and O. Lebedev, *First LHC constraints on neutralinos*, *Phys. Lett. B* **715** (2012) 199 [[arXiv:1206.3096](#)] [[INSPIRE](#)].
- [89] A. Choudhury and A. Datta, *Neutralino dark matter confronted by the LHC constraints on electroweak SUSY signals*, *JHEP* **09** (2013) 119 [[arXiv:1305.0928](#)] [[INSPIRE](#)].
- [90] L. Calibbi, T. Ota and Y. Takanishi, *Light neutralino in the MSSM: a playground for dark matter, flavor physics and collider experiments*, *JHEP* **07** (2011) 013 [[arXiv:1104.1134](#)] [[INSPIRE](#)].
- [91] G. Belanger et al., *Lower limit on the neutralino mass in the general MSSM*, *JHEP* **03** (2004) 012 [[hep-ph/0310037](#)] [[INSPIRE](#)].
- [92] G. Belanger et al., *SUSY Higgs at the LHC: effects of light charginos and neutralinos*, *Nucl. Phys. B* **581** (2000) 3 [[hep-ph/0002039](#)] [[INSPIRE](#)].
- [93] R.K. Barman et al., *Invisible decay of the Higgs boson in the context of a thermal and nonthermal relic in MSSM*, *Phys. Rev. D* **95** (2017) 095018 [[arXiv:1703.03838](#)] [[INSPIRE](#)].
- [94] M. Chakraborti, U. Chattopadhyay and S. Poddar, *How light a higgsino or a wino dark matter can become in a compressed scenario of MSSM*, *JHEP* **09** (2017) 064 [[arXiv:1702.03954](#)] [[INSPIRE](#)].
- [95] I. Hinchliffe and T. Kaeding, *B+L violating couplings in the minimal supersymmetric standard model*, *Phys. Rev. D* **47** (1993) 279 [[INSPIRE](#)].

- [96] G. Bhattacharyya and P.B. Pal, *New constraints on R-parity violation from proton stability*, *Phys. Lett. B* **439** (1998) 81 [[hep-ph/9806214](#)] [[INSPIRE](#)].
- [97] L.E. Ibanez and G.G. Ross, *Discrete gauge symmetry anomalies*, *Phys. Lett. B* **260** (1991) 291 [[INSPIRE](#)].
- [98] H.K. Dreiner, C. Luhn and M. Thormeier, *What is the discrete gauge symmetry of the MSSM?*, *Phys. Rev. D* **73** (2006) 075007 [[hep-ph/0512163](#)] [[INSPIRE](#)].
- [99] H.K. Dreiner, C. Luhn, H. Murayama and M. Thormeier, *Baryon triality and neutrino masses from an anomalous flavor U(1)*, *Nucl. Phys. B* **774** (2007) 127 [[hep-ph/0610026](#)] [[INSPIRE](#)].
- [100] H.K. Dreiner, M. Hanussek and C. Luhn, *What is the discrete gauge symmetry of the R-parity violating MSSM?*, *Phys. Rev. D* **86** (2012) 055012 [[arXiv:1206.6305](#)] [[INSPIRE](#)].
- [101] S.P. Martin, *A supersymmetry primer*, *Adv. Ser. Direct. High Energy Phys.* **18** (1998) 1 [[hep-ph/9709356](#)] [[INSPIRE](#)].
- [102] R.N. Mohapatra, *Supersymmetry and R-parity: an overview*, *Phys. Scripta* **90** (2015) 088004 [[arXiv:1503.06478](#)] [[INSPIRE](#)].
- [103] J.L. Goity and M. Sher, *Bounds on $\Delta B = 1$ couplings in the supersymmetric standard model*, *Phys. Lett. B* **346** (1995) 69 [Erratum *ibid.* **385** (1996) 500] [[hep-ph/9412208](#)] [[INSPIRE](#)].
- [104] F. Zwirner, *Observable $\Delta B = 2$ transitions without nucleon decay in a minimal supersymmetric extension of the standard model*, *Phys. Lett. B* **132** (1983) 103 [[INSPIRE](#)].
- [105] I. Zurbano Fernandez et al., *High-Luminosity Large Hadron Collider (HL-LHC): technical design report*, CERN-2020-010, CERN, Geneva, Switzerland (2020) [[DOI:10.23731/CYRM-2020-0010](#)] [[INSPIRE](#)].
- [106] CMS collaboration, *The phase-2 upgrade of the CMS level-1 trigger*, CERN-LHCC-2020-004, CERN, Geneva, Switzerland (2020).
- [107] CMS collaboration, *The phase-2 upgrade of the CMS barrel calorimeters*, CERN-LHCC-2017-011, CERN, Geneva, Switzerland (2017).
- [108] CMS, collaboration, *A MIP timing detector for the CMS phase-2 upgrade*, CERN-LHCC-2019-003, CERN, Geneva, Switzerland (2019).
- [109] CMS collaboration, *The phase-2 upgrade of the CMS endcap calorimeter*, CERN-LHCC-2017-023, CERN, Geneva, Switzerland (2017) [[DOI:10.17181/CERN.IV8M.1JY2](#)].
- [110] PARTICLE DATA GROUP collaboration, *Review of particle physics*, *PTEP* **2022** (2022) 083C01 [[INSPIRE](#)].
- [111] J. Fiaschi, B. Fuks, M. Klasen and A. Neuwirth, *Electroweak superpartner production at 13.6 TeV with Resummino*, *Eur. Phys. J. C* **83** (2023) 707 [[arXiv:2304.11915](#)] [[INSPIRE](#)].
- [112] LHC SUSY X-SECTION WG, *Cross sections for various subprocesses — 14 TeV*, <https://twiki.cern.ch/twiki/bin/view/LHCPhysics/SUSYCrossSections>.
- [113] C. Bierlich et al., *A comprehensive guide to the physics and usage of PYTHIA 8.3*, *SciPost Phys. Codeb.* **2022** (2022) 8 [[arXiv:2203.11601](#)] [[INSPIRE](#)].
- [114] D. Stump et al., *Inclusive jet production, parton distributions, and the search for new physics*, *JHEP* **10** (2003) 046 [[hep-ph/0303013](#)] [[INSPIRE](#)].
- [115] CMS collaboration, *Event generator tunes obtained from underlying event and multiparton scattering measurements*, *Eur. Phys. J. C* **76** (2016) 155 [[arXiv:1512.00815](#)] [[INSPIRE](#)].

- [116] J. Alwall et al., *The automated computation of tree-level and next-to-leading order differential cross sections, and their matching to parton shower simulations*, *JHEP* **07** (2014) 079 [[arXiv:1405.0301](#)] [[INSPIRE](#)].
- [117] R. Frederix et al., *The automation of next-to-leading order electroweak calculations*, *JHEP* **07** (2018) 185 [*Erratum ibid.* **11** (2021) 085] [[arXiv:1804.10017](#)] [[INSPIRE](#)].
- [118] DELPHES 3 collaboration, *DELPHES 3, a modular framework for fast simulation of a generic collider experiment*, *JHEP* **02** (2014) 057 [[arXiv:1307.6346](#)] [[INSPIRE](#)].
- [119] M. Cacciari, G.P. Salam and G. Soyez, *The anti- k_t jet clustering algorithm*, *JHEP* **04** (2008) 063 [[arXiv:0802.1189](#)] [[INSPIRE](#)].
- [120] CMS collaboration, *CMS the TriDAS project: technical design report, volume 2. Data acquisition and high-level trigger. CMS trigger and data-acquisition project*, CERN-LHCC-2002-026, CERN, Geneva, Switzerland (2002).
- [121] CMS collaboration, *The CMS trigger system*, 2017 *JINST* **12** P01020 [[arXiv:1609.02366](#)] [[INSPIRE](#)].
- [122] CMS collaboration, *The phase-2 upgrade of the CMS data acquisition and high level trigger*, CERN-LHCC-2021-007, CERN, Geneva, Switzerland (2021).
- [123] E. Govorkova et al., *Autoencoders on field-programmable gate arrays for real-time, unsupervised new physics detection at 40 MHz at the Large Hadron Collider*, *Nature Mach. Intell.* **4** (2022) 154 [[arXiv:2108.03986](#)] [[INSPIRE](#)].
- [124] M. Neu et al., *Real-time graph building on FPGAs for machine learning trigger applications in particle physics*, [arXiv:2307.07289](#) [[INSPIRE](#)].
- [125] CMS collaboration, *First level track jet trigger for displaced jets at High Luminosity LHC*, CMS-PAS-FTR-18-018, CERN, Geneva, Switzerland (2018).
- [126] M. Tosi, *Tracking at ATLAS and CMS with special emphasis on run-2 performance and developments for run-3*, in *LHCP 2021*, <https://indi.to/pKVCq>, 10 June 2021.
- [127] T. Chen and C. Guestrin, *XGBoost: a scalable tree boosting system*, in *Proceedings of the 22nd ACM SIGKDD international conference on knowledge discovery and data mining*, KDD '16, New York, NY, U.S.A. (2016), p. 785 [[DOI:10.1145/2939672.2939785](#)] [[arXiv:1603.02754](#)] [[INSPIRE](#)].